Preprint Cambridge Centre for Computational Chemical Engineering ISSN 1473 – 4273

Co_3O_4 and $Fe_xCo_{3-x}O_4$ nanoparticles/films synthesized in a vapor-fed flame aerosol reactor for oxygen evolution

Yuan Sheng [1], Maria L. Botero [2], Manoel Y. Manuputty [3], Markus Kraft [1,3], Rong Xu [1]

released: 8 November 2017

[1] School of Chemical and Biomedical Engineering
Nanyang Technological University
62 Nanyang Drive
637459
Singapore
Email: rxu@ntu.edu.sg

[2] Department of Mechanical Engineering
National University of Singapore
9 Engineering Drive 1
117575
Singapore

[3] Department of Chemical Engineering and Biotechnology
University of Cambridge
West Cambridge Site
Philippa Fawcett Drive
Cambridge, CB3 0AS
United Kingdom
E-mail: mk306@cam.ac.uk

Preprint No. 193

UNIVERSITY OF CAMBRIDGE

Keywords: nanomaterial, flame synthesis, thin film, Co_3O_4, doping, oxygen evolution reaction, premixed stagnation flame

Edited by
Computational Modelling Group
Department of Chemical Engineering and Biotechnology
University of Cambridge
West Cambridge Site
Philippa Fawcett Drive
Cambridge CB3 0AS
United Kingdom

Fax: + 44 (0)1223 334796
E-Mail: c4e@cam.ac.uk
World Wide Web: http://como.cheng.cam.ac.uk/

Abstract

Synthesis of earth-abundant nanocatalysts for the oxygen evolution reaction (OER) has depended largely on highly diluted, batchwise wet chemical methods, leaving it a challenge to improve throughput and sustainability of the process. Herein, we demonstrate for the first time the production of Co_3O_4 and $Fe_xCo_{3-x}O_4$ nanoparticles using vapor-fed flame aerosol synthesis (VFAS), a continuous and scalable process requiring minimal waste treatment. In 1M KOH, the catalysts exhibit stable OER overpotentials of 295 mV @ 10 mA/cm^2 and Tafel slopes down to 38 mV/dec, which are comparable to the performances of wet-chemically derived benchmark (Fe-doped) Co_3O_4 catalysts. The high activity is attributed to ultrafine particle size of $\langle D_p \rangle$ = 3.1-4.4 nm and rich surface defects. Furthermore, nanostructured Co_3O_4 and $Fe_xCo_{3-x}O_4$ films can be conveniently grown on graphite substrates by VFAS and serve as OER electrodes without further treatment. Remarkably, the morphology of the films can be easily tuned from columnar to granular by varying precursor concentration in feed gas, achieving optimal utilization of catalytic materials with a hierarchical structure consisting of elongated nanoparticulate building blocks.

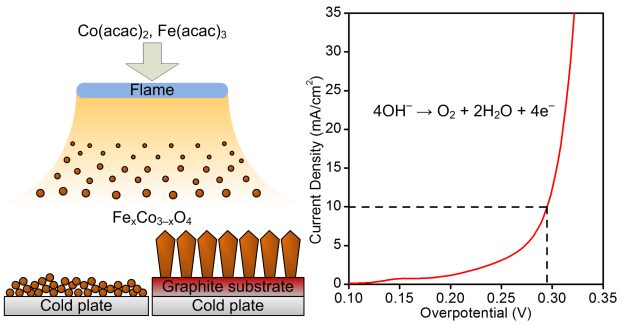

Highlights

- Co_3O_4 and $Fe_xCo_{3-x}O_4$ nanoparticles/nanostructured films were prepared by vapor-fed flame aerosol synthesis for the first time.
- The morphology of the films was tunable from columnar to granular by changing precursor concentration in the flame mixture.
- The nanoparticles exhibited a comparable electrocatalytic oxygen evolution activity with that of wet-chemically synthesized benchmarks.
- The as-prepared catalyst films can serve as water splitting electrodes directly without further treatment.

Contents

1 Introduction

Hydrogen production by solar-driven water splitting has been considered a promising technology to mitigate environmental problems associated with increasing consumption of fossil fuels [53]. Between the two half reactions of water splitting, i.e. hydrogen evolution reaction (HER) and oxygen evolution reaction (OER), the kinetically more sluggish four-electron OER limits the overall reaction rate by a high overpotential [20]. To reduce the energy penalty caused by the overpotential and pave the way for industrialization of the technology, highly efficient cost-effective OER catalysts are urgently needed [37]. While the established noble metal catalysts such as RuO_2 and IrO_2 exhibit satisfactory OER activity [24], their high cost prevents large-scale applications.

For more than three decades, intensive research has been conducted on the development of earth-abundant OER catalysts for low cost [46, 52]. Particularly, nanosized Co oxides and (oxy)hydroxides show encouraging OER activity and stability in alkaline electrolytes [57]. With continuous efforts to optimize their electrochemical properties, state-of-the-art Co-based catalysts have outperformed the noble metal benchmarks. For example, size reduction of Co_3O_4 spinel nanoparticles and exfoliation of Co-based layered double hydroxide (LDH) have been proven effective in enhancing OER activity by exposing more active sites [14, 44]. To improve electrical conductivity of such catalysts and hence increase accessibility of the surface active sites, syntheses of 3-D hierarchical structures and composites with conductive carbon materials have also yielded positive results [43, 58, 62, 71–74]. Furthermore, the considerable flexibility in chemical composition of spinel allows for facile introduction of defect sites and dopant elements including Fe, Ni, and Zn to the Co-based system to generate highly active OER sites [4, 11, 12, 17, 18, 59, 60, 65, 75]. Recent studies on Co-based spinel materials have demonstrated different reactivity of Co^{2+} and Co^{3+} centers during OER [35, 56]. Despite controversies among the results, they nevertheless suggest an additional degree of control in enhancing the performance of Co-based spinel catalysts.

In contrast to the fast advancing performance of nanostructured OER catalysts in laboratory research, feasibility of their synthesis methods in an industrial context has received little attention. So far wet chemical methods such as hydrothermal and solvothermal treatments sometimes followed by heat treatment have dominated the synthesis of OER catalysts. For optimal size and morphology of the nanomaterials, a typical reaction mixture is highly diluted which leads to low throughput. The synthesis suffers further from long process cycles and energy-intensive separation, and generates a large amount of waste water. Although in situ electrochemical synthesis of OER catalysts simplified the manufacturing process and the electrodes have shown good performance [38, 67], treatment of hazardous waste water is still a cause of concern. Importantly, all the methods above are batch processes.

Flame aerosol synthesis (FAS) is an industrially relevant method of producing nanoparticles. In FAS, precursors are continuously fed to and pyrolyzed in a flame where particles form in the gas phase from pyrolysis products. Depending on the physical state of the precursors upon introduction to the flame, the FAS process can be categorized as vapor-fed (VFAS) or liquid-fed (LFAS) [27]. Steam, CO_2, excess O_2 and inert carrier gas (e.g. N_2 or Ar) are typically the only components of the exhaust of FAS using an oxidative flame.

Compared with the batch process of wet-chemical synthesis, FAS involves fewer unit operations, shorter processing time and simpler waste treatment, and is hence more suitable for high-throughput production in commercial scale [23, 39]. Indeed, FAS accounts for the production of most commodity nanoparticles including carbon black, fumed SiO_2 and TiO_2 which FAS was first developed for [42]. Its scope has since been expanded to the synthesis of numerous nanomaterials including most non-radioactive metal oxides, noble metals, carbon, and their composites [27, 36]. Moreover, nanostructured films such as TiO_2, ZnO, SnO_2 and rare earth oxides have been successfully deposited by FAS in open atmosphere and applied in fuel cells, solar cells, Li-ion batteries, water splitting and gas sensing [6, 30, 40, 41, 49, 64, 68]. It suggests FAS to be a fast and low-cost alternative to chemical vapor deposition in mass production of catalytic films. VFAS in particular is capable of producing ultrafine nanoparticles with narrow size distribution and nanostructured films with tunable morphology [49, 69], which are important advantages in designing OER catalysts. However, to the best of our knowledge the use of FAS-derived Co oxides in OER has not been reported. In fact, examples of FAS of Co oxides are scarce in general, and the few published works adopted LFAS exclusively [2, 22, 28, 47].

Herein, we prepare pure and Fe-doped Co_3O_4 spinel by VFAS and demonstrate their high activity in OER. For comparison with wet-chemically synthesized analogues, the flame-synthesized materials are first studied in the form of free-standing nanoparticles. The unique advantages of VFAS are then explored by growing nanostructured films at different precursor concentrations, which leads to tunable film morphologies. Finally, the as-synthesized films are directly evaluated as OER working electrodes.

2 Experimental methodology

2.1 Chemicals

Iron(III) acetylacetonate ($Fe(acac)_3$, 97%), cobalt(II) acetylacetonate ($Co(acac)_2$, 97%), potassium hydroxide (KOH, ACS Reagent), Nafion perfluorinated resin solution (5%), iron standard solution (1000 mg/L), and cobalt standard solution (1000 mg/L) from Sigma-Aldrich, ethylene (C_2H_4, 99.9%), hydrogen (H_2, purified), oxygen (O_2, purified), nitrogen (N_2, purified), and argon (Ar, purified) from Air Liquide, absolute ethanol (EtOH, for synthesis), 2-propanol (IPA, for analysis), nitric acid (HNO_3, 65% for analysis), and hydrochloric acid (HCl, 37% for analysis) from Merck were used as received.

2.2 Synthesis

Co_3O_4 and $Fe_xCo_{3-x}O_4$ were synthesized in a flame aerosol reactor at atmospheric pressure. The burner was supplied by Hestia Tec, LLC [50]. A schematic diagram can be found in **Figure S1**. Briefly, an Ar stream preheated to 90 °C was allowed to pass through an electrically heated sublimator filled with $Co(acac)_2$ or a $Co(acac)_2$/$Fe(acac)_3$ mixture to carry the precursor vapors to a premixed C_2H_4/O_2/Ar stagnation flame with an equivalence ratio ϕ = 0.25. The equivalence ratio is defined as $\phi = \frac{Q_{C_2H_4}/Q_{O_2}}{\nu_{C_2H_4}/\nu_{O_2}}$, where $Q_{C_2H_4}$ and

Q_{O_2} are the volumetric flow rates of the two gases in standard condition and $v_{C_2H_4}/v_{O_2}$ is the stoichiometric ratio for complete combustion of C_2H_4 which equals to 1/3. The sublimator was kept at 115, 120 or 125 °C. The flame impinged on a water cooled aluminum stagnation plate (**Figure 1**) which reached a surface temperature of 150 °C at steady state. Free-standing nanoparticles were collected from the plate after the flame was turned off and the plate was cooled down in laboratory air. Pure Co_3O_4 powder samples (synthesized without $Fe(acac)_3$ loaded in the sublimator) are denoted by Co115C, Co120C or Co125C and Fe-doped samples by CoFe115C, CoFe120C, or CoFe125C depending on the sublimator temperature used. Nanostructured Co_3O_4 and $Fe_xCo_{3-x}O_4$ films were prepared by inserting a 5×30 mm graphite substrate (0.5 mm thick, >99.5%, Latech Scientific Supply) between the flame and the stagnation plate. The substrate reached a surface temperature of 570 °C due to limited heat transfer from the substrate to the stagnation plate. After 5 min of deposition the substrate was removed and cooled down in laboratory air. The pure Co_3O_4 films are denoted by Co115C5min, Co120C5min, or Co125C5min and Fe-doped films by CoFe115C5min, CoFe120C5min, or CoFe125C5min depending on the sublimator temperature used. Detailed description of the set-up and the procedure can be found in Appendix A.

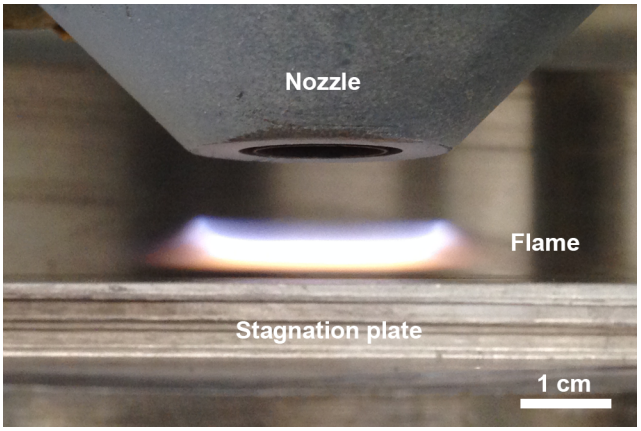

Figure 1: *Photograph of a typical flame during the synthesis of Co_3O_4 nanoparticles.*

2.3 Materials Characterization

Morphology of the Co_3O_4 and $Fe_xCo_{3-x}O_4$ nanoparticles/films was studied by transmission electron microscopy (TEM, JEM-2100F, 200 kV) and scanning electron microscopy (SEM, JSM-6700F, 5 kV). Crystallographic information was obtained by X-ray diffraction (XRD, Bruker D8 Advance) using a Cu Kα source with a wavelength of 1.54 Å. Surface chemical states were studied by X-ray photoelectron spectroscopy (XPS, Kratos AXIS Ultra DLD) using a monochromated Al Kα source with an X-ray energy of 1486.7 eV. The 1*s* binding energy of sp^3 adventitious carbon, set to 284.8 eV, was used for charge referencing. Elemental composition was analyzed by inductively coupled plasma optical emission spectroscopy (ICPOES, Thermo Scientific iCAP 6200 Duo). The samples were digested with aqua regia at 60 °C for 2 h and diluted with deionized water before analysis.

2.4 Electrode Preparation

For the powder samples, 5 mg of as-synthesized nanoparticles was dispersed in a mixture of 1 mL of 75 vol% IPA solution and 6 μL of 5% Nafion solution to form a homogeneous ink with the aid of an ultrasonic bath. 50 μL of such catalyst ink was drop-casted onto a 5×5 mm Ni foam electrode (1 mm thick, 100-110 pores/inch, >99% Ni, Latech Scientific Supply) and dried at 50 °C for 2 h (**Figure S2**). For the film samples, as-prepared graphite electrodes were coated with epoxy resin, leaving only a 5×5 mm area of catalyst film and a portion of bare graphite of similar size (for electrical contact with the potentiostat) exposed. The electrodes were directly used as working electrodes after the resin cured (**Figure S3**).

2.5 Electrochemical Measurement

Electrochemical experiments were performed at room temperature in a three-electrode cell using 1M KOH as the electrolyte, Ag/AgCl/3M KCl as the reference electrode, and Pt sheet as the counter electrode. The reference electrode was calibrated in H_2-saturated 1M KOH using Pt wire as the working electrode. OER activity was evaluated by cyclic voltammetry (CV) and linear sweep voltammetry (LSV) techniques (Metrohm Autolab PGSTAT302N), and uncompensated resistance was determined by electrochemical impedance spectroscopy (Metrohm Autolab FRA32M) at 1.23 V vs RHE with 10 mV sinusoidal perturbation voltage. The electrolyte was saturated with continuous bubbling of O_2. 25 CV scans at 100 mV/s were first performed to achieve a stable voltammogram. A LSV scan at 5 mV/s was then used to determine the overpotential required for 10 mA/cm^2 OER current density. Another LSV scan at 0.25 mV/s was finally performed to measure Tafel slope near the current density of 10 mA/cm^2. Catalyst stability was tested by chronopotentiometry over 200 min of continuous electrolysis at 10 mA/cm^2 after the LSV measurements. 95% *iR* compensation was adopted during the performance evaluation.

2.6 Computational Method

The flame temperature was calculated by the *k*inetics® software package [1, 33] using the reaction model proposed by Wang et al. [55].

3 Results and Discussion

3.1 Free-Standing Co_3O_4 and $Fe_xCo_{3-x}O_4$ Nanoparticles

Co_3O_4 and $Fe_xCo_{3-x}O_4$ nanoparticles were synthesized in the same $C_2H_4/O_2/Ar$ flame with an equivalence ratio $\phi = 0.25$. The precursor sublimator was loaded with either pure $Co(acac)_2$ or a 1:1 mixture of $Co(acac)_2/Fe(acac)_3$ and held at three different temperatures: 115, 120 and 125 °C to study the effects of precursor concentration in the flame mixture.

The adiabatic flame temperature was calculated to be 1930 K. The effects of metal precursors on equivalence ratio and flame temperature were ignored due to their low concentrations. As shown in **Figure 1**, in all synthesis experiments an orange colored region with a thickness of ~3 mm is visible in the immediate downstream of the flame front, which cannot be observed in a precursor-free flame and is attributed to nanoparticles emitting thermal radiation. The intensity of thermal radiation drops sharply as the flame mixture reaches a zone within 0.8 mm from the stagnation surface. The observation is consistent with reported axial temperature profile of similar premixed stagnation flames which indicated rapid cooling of the flame mixture (in the order of 10^3 K/mm) only in a thin zone near the stagnation surface [50]. Collision of the nanoparticles with gas molecules of different kinetic energies results in a net force down the temperature gradient and drives diffusion of the nanoparticles known as thermophoresis, which contributes significantly to the deposition of the nanoparticles as thermophoresis dominates their movement towards the stagnation surface in the boundary layer [50, 70]. Thermophoresis was maximized in the synthesis of Co_3O_4 and $Fe_xCo_{3-x}O_4$ nanoparticles by keeping the stagnation plate at a low temperature.

From here onwards, the nanoparticle products are referred to as Co115C, Co120C, Co125C, CoFe115C, CoFe120C and CoFe125C depending on the temperature of the precursor sublimator (the 3 digits in the sample names) and whether Fe precursor was introduced. After 30 min of synthesis, about 14 mg of Co115C could be recovered from the stagnation plate and the amount increased to 25 mg for Co125C, reflecting the increase in vapor pressure and hence gas-phase concentration of the precursor with temperature of the sublimator.

The powder XRD patterns of the six nanoparticle samples in **Figure 2** exhibit broad diffraction peaks that can be assigned to the spinel structure. No other crystalline phases are detected. The positions of the diffraction peaks of the three Fe-free samples closely match those of bulk Co_3O_4 in reference pattern (PDF #42-1467, space group $Fd\bar{3}m$, $a = 8.08$ Å). Therefore Co115C, Co120C and Co125C are determined to be phase-pure Co_3O_4. Doping with Fe results in shifting of diffraction peaks towards lower 2θ angles but no phase change, indicating expansion of the Co_3O_4 lattice to accommodate the Fe dopant. Interestingly, the lattice constant of the $Fe_xCo_{3-x}O_4$ calculated from the diffraction data is $a = 8.16$-8.18 Å (**Table S1**), lying between that of Co_3O_4 ($a = 8.08$ Å) and $CoFe_2O_4$ spinel (PDF #22-1086, space group $Fd\bar{3}m$, $a = 8.39$ Å). It suggests that the $Fe_xCo_{3-x}O_4$ samples obtained in this work are solid solutions of the two phases. The Co/Fe ratio derived from the lattice constant using Vegard´s law is 3.7-4.8 which is in good agreement with the elemental composition determined by ICPOES and XPS (**Table 1**). Average crystallite sizes calculated from the full width at half maximum of the strongest (311) diffraction peaks are also presented in **Table 1**. The sizes, ranging from 3.8 nm to 5.4 nm, are up to 9.5 times smaller than that of Co_3O_4 nanoparticles synthesized by a liquid-fed system [2] and are comparable to the sizes achieved in state-of-the-art Co_3O_4 nanocatalysts synthesized by wet chemistry [10, 25, 65]. A comparison between the crystallite sizes obtained at increasing temperature of the precursor sublimator reveals an increasing trend in both Co_3O_4 and $Fe_xCo_{3-x}O_4$ particles. Consistent results are obtained when different diffraction peaks are used to calculate the crystallite sizes (**Table S1**). The trend can be mainly attributed to higher precursor concentration, as reported in VFAS of TiO_2 [69]. In contrast, the Co/Fe ratio and diffraction line positions of the $Fe_xCo_{3-x}O_4$ samples are insensitive to the temperature of the precursor sublimator, which indicates increases

in the gas-phase concentrations of $Co(acac)_2$ and $Fe(acac)_3$ by similar proportions with temperature.

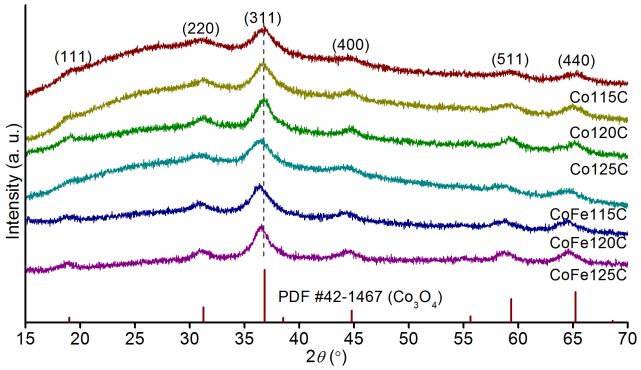

Figure 2: *Powder XRD patterns of the free-standing Co_3O_4 and $Fe_xCo_{3-x}O_4$ nanoparticles.*

Table 1: *Physicochemical properties and OER performance of Co_3O_4 and $Fe_xCo_{3-x}O_4$ particles*

Catalyst	η_{10} (mV) [a]	Tafel slope (mV/dec)	J_0 (mA/cm^2) [b]	Bulk Co/Fe [c]	Surface Co/Fe [d]	Crystallite size (nm) [e]	$\langle D_p \rangle$ (nm) [f]	σ [g]	Co1/Co2 [d]	O2% [d]
Co115C	300	56	3.3×10^{-5}	∞	∞	3.9	3.3	1.24	0.72	33
Co120C	299	55	2.8×10^{-5}	∞	∞	4.8	3.9	1.26	0.71	32
Co125C	301	56	3.0×10^{-5}	∞	∞	5.0	4.2	1.24	0.75	31
CoFe115C	295	39	3.5×10^{-7}	5.0	4.2	3.8	3.1	1.25	0.63	56
CoFe120C	299	39	1.9×10^{-7}	4.3	3.8	4.3	3.5	1.25	0.62	59
CoFe125C	301	38	1.2×10^{-7}	4.4	4.0	5.4	4.4	1.30	0.61	54

[a] η_{10}: overpotential at 10 mA/cm^2; [b] J_0: exchange current density; [c] determined by ICPOES; [d] determined by XPS; [e] determined by XRD; [f] $\langle D_p \rangle$: geometric mean particle size determined by TEM; [g] σ: geometric standard deviation of particle size determined by TEM.

Figure 3 presents high-resolution TEM images of Co_3O_4 and $Fe_xCo_{3-x}O_4$ nanoparticles. In general, the particles are crystalline without noticeable amorphous surface layers or domains. All the six samples appear as truncated spheres/spheroids. More developed crystal facets can be observed in Co125C and CoFe125C, but well-defined polyhedrons do not form. Lattice fringes with d-spacing values corresponding to the phases identified by XRD can be readily observed in all samples which extend continuously through individual primary particles. Despite certain degree of aggregation, it is apparent that the primary particles are single crystals. The slightly larger d-spacing of (400) planes in the $Fe_xCo_{3-x}O_4$ samples also reflects the lattice expansion due to Fe doping, although with a limited spatial resolution of 1 Å the TEM analysis provides less definite crystallographic information than does the XRD technique. The Co_3O_4 and $Fe_xCo_{3-x}O_4$ particles synthesized at the same sublimator temperatures are otherwise similar under TEM observation. For comparison with the crystallite sizes calculated from the XRD data, particle sizes were determined by directly measuring at least 500 particles on the TEM images of each sample (**Figure S4** shows examples of the images used for analysis). According to the

histograms in the insets of **Figure 3**, the particles have a unimodal distribution. Their geometric mean sizes ($\langle D_p \rangle$ in **Table 1**) have reasonable agreement with the XRD-derived crystallite sizes, corroborating the single crystalline nature of the nanoparticles. The geometric standard deviations (σ) are much smaller compared with that of a self-preserving size distribution of coalescing aerosols ($\sigma \simeq 1.45$), indicating insignificant coalescence during particle growth as a result of the short residence time in flame [50].

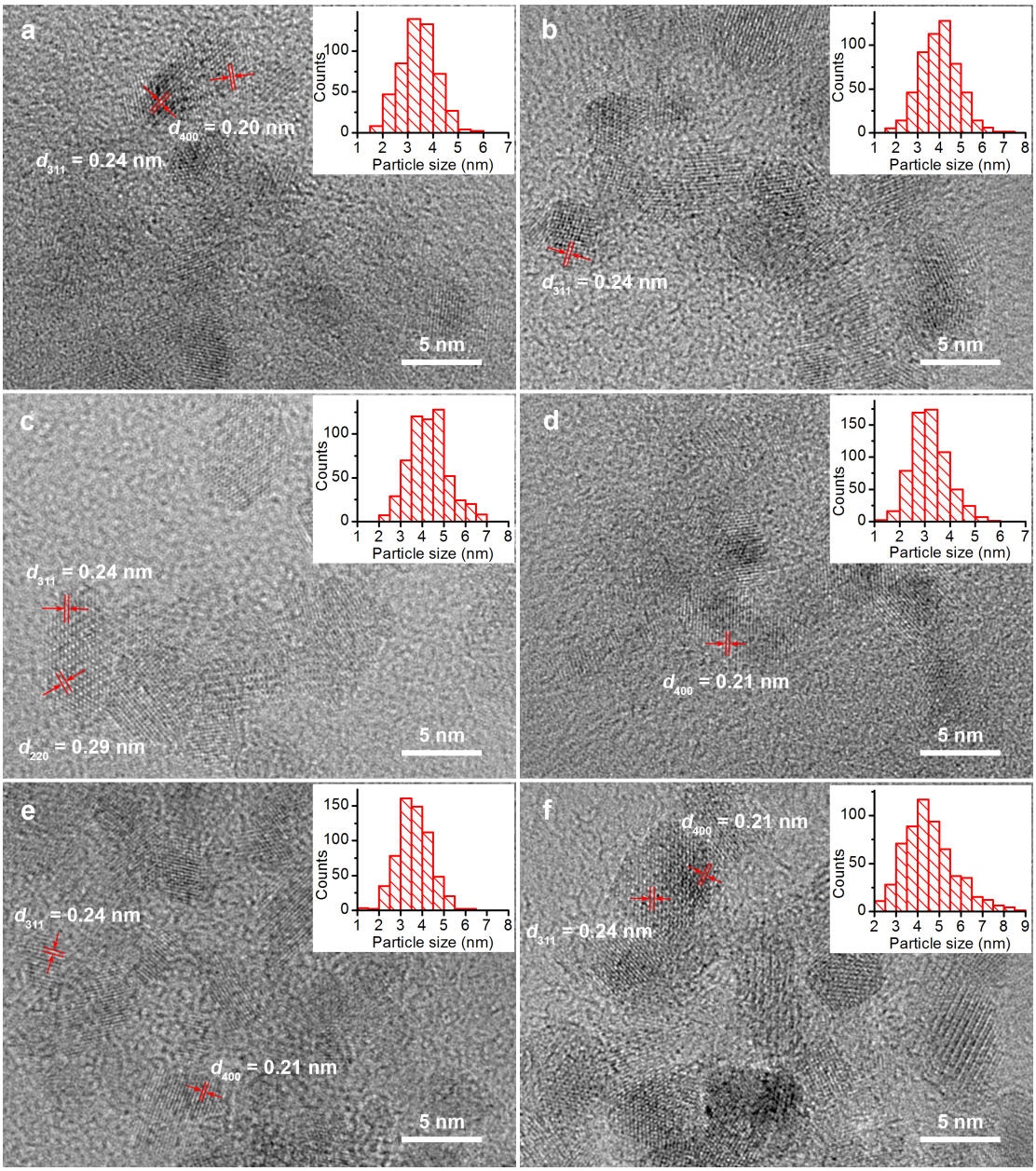

Figure 3: *High-resolution TEM images of (a) Co115C, (b) Co120C, (c) Co125C, (d) CoFe115C, (e) CoFe120C, and (f) CoFe125C. Insets: particle size histograms.*

The OER activity of the flame-synthesized Co_3O_4 and $Fe_xCo_{3-x}O_4$ nanoparticles is tested on supporting electrodes composed of Ni foam. The linear sweep voltammetry (LSV) results in **Figure 4a** show different anodic waves in the pre-OER region for the pure and Fe-

doped Co_3O_4 catalysts. The three pure Co_3O_4 samples exhibit a broad major wave located around an OER overpotential of 0.23 V (1.46 V vs RHE) and a weak shoulder around an OER overpotential of 0.13 V (1.36 V vs RHE), which can be assigned to oxidation of Co(III) to Co(IV) in the catalyst particles and Ni(II) to Ni(III) on the exposed surface of Ni foam, respectively [8, 9]. For the Fe-doped samples, however, the Co(III)/Co(IV) wave cannot be discerned and the Ni(II)/Ni(III) wave is shifted anodically by 25 mV. Electronic effects of Fe dopant on Co- and Ni-based catalysts which lead to anodic shifts in pre-OER redox waves have been well documented [7, 51]. It is probable that the large degree of Fe doping achieved in this work causes the Co(III)/Co(IV) waves to be strongly shifted and overlap with the OER waves [45]. Similarly, the shift of the Ni(II)/Ni(III) wave is attributed to migration of Fe species from the catalyst particles to the Ni foam. The extent of the shift is much lower than that of the Co(III)/Co(IV) waves, being comparable to a shift resulting from contact with an electrolyte containing trace amount of Fe impurities [51]. It should be noted that the Ni(II)/Ni(III) redox waves emerged slowly during the stabilizing cyclic voltammetry (CV) scans without increase in OER current, which indicates minimal contribution of the surface Ni species to overall OER activity. Indeed, the onset of OER occurs at a much more anodic potential without loading the Ni foam with the catalyst particles. As summarized in **Table 1**, all six samples exhibit high OER activity, requiring as low as 295 mV of overpotential to achieve the current density of 10 mA/cm^2 (η_{10}) which is comparable to the performance of some of the best wet-chemically synthesized Co_3O_4-based nanocatalysts listed in **Table S2**. Furthermore, **Figure 4b** shows good stability of the most active catalyst CoFe115C; the increase in OER overpotential during the 200 min chronopotentiometric experiment at 10 mA/cm^2 is less than 1 mV. Although the difference in overpotential is small among the six catalysts, a slight increasing trend seems to exist with increasing sublimator temperature, reflecting the inverse correlation between apparent activity and particle size [14]. Regardless of sublimator temperature, the Co_3O_4 and $Fe_xCo_{3-x}O_4$ nanoparticles exhibit Tafel slopes of 55-56 mV/dec and 38-39 mV/dec respectively, outperforming most wet-chemically synthesized benchmark catalysts (**Table S2**). While the reduction in Tafel slope indicates formation of highly active catalytic centers upon the introduction of Fe as expected [59], the positive effect of Fe on reducing overpotential only becomes apparent at current densities beyond 10 mA/cm^2. Extrapolation from the Tafel plots (**Figure S5**) reveals that the exchange current densities (J_0) of the $Fe_xCo_{3-x}O_4$ samples are two orders of magnitude lower than those of the pure Co_3O_4 samples (**Table 1**), which suggests a lower density of exposed active sites in the former. It can be explained by in situ formation of poorly conductive Fe (oxy)hydroxide species on the catalytic surfaces that limits electrical access to the active sites [7].

To further understand the factors in the OER activity of the flame-synthesized nanoparticles, surface chemical states of O, Fe and Co are studied by X-ray photoelectron spectroscopy (XPS). The Co $2p_{3/2}$ spectra in **Figure 5a** can be deconvoluted into 5 component peaks at binding energies consistent with those of a reference Co_3O_4 sample, as listed in **Table S3** [5]. The ratio between the areas of the two major peaks located at 779.8 eV (Co1) and 780.8 eV (Co2) decreases from about 0.73 to 0.62 with the introduction of Fe dopant (**Table 1**), which translates into a decrease in the relative amount of Co^{3+} as the Co1 and Co2 peaks have been assigned to Co^{3+} and Co^{2+}, respectively [4, 75]. To explain such a decrease, the chemical state of Fe in $Fe_xCo_{3-x}O_4$ is examined by Fe $3p$ spectra presented in **Figure 5c** (a strong signal from Co LMM Auger electrons overlaps with the

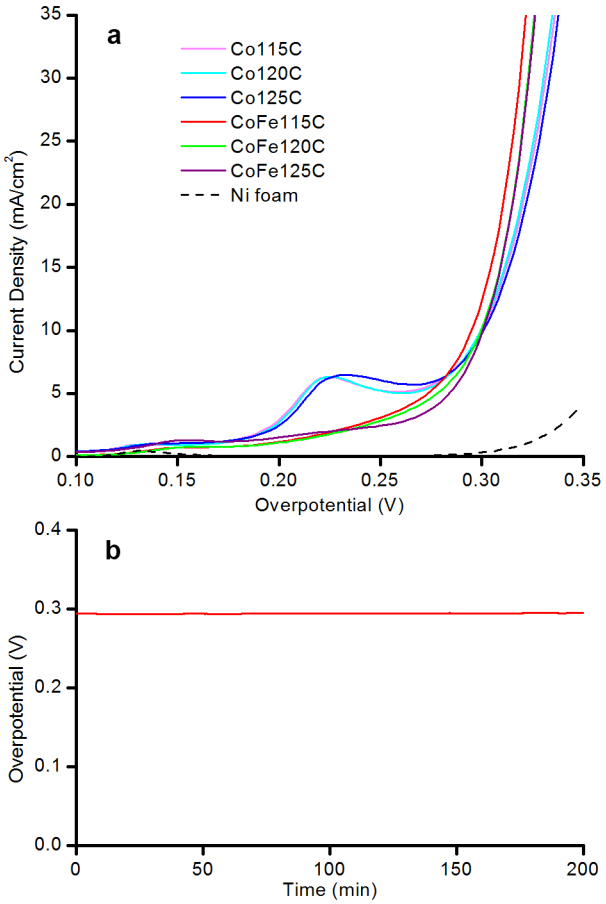

Figure 4: *(a) LSV curves from OER tests on the Co_3O_4 and $Fe_xCo_{3-x}O_4$ particles supported on Ni foam, and (b) chronopotentiometric curve for CoFe115C at 10 mA/cm^2.*

more widely studied Fe 2*p* spectra and prevents accurate analysis, see **Figure S6**). Due to close proximity of Co 3*p* signals, deconvolution of the Fe/Co 3*p* spectra is performed simultaneously (**Table S4**). It can be seen that only one chemical state of Fe is resolved at the binding energy of 55.7 eV, assigned to Fe^{3+} [34]. Preferential substitution of Co^{3+} by Fe^{3+} is therefore the most likely reason for the change in Co1/Co2 ratio. In addition, we note that both the flame-synthesized Co_3O_4 and $Fe_xCo_{3-x}O_4$ have Co1/Co2 ratios much lower than the value of 1.39 for bulk Co_3O_4 reference [5], which suggests a more reduced surface compared with that of an ideal phase. We attribute the reduced state to the unique temperature history of the nanoparticles in our VFAS set-up. During the majority of their residence time in flame, the particles are subjected to near-maximum flame temperature due to inefficient heat transfer from the laminar flame to the stagnation surface [50]. The maximal temperature of such a flame is usually close to the adiabatic flame temperature which in this work is 1930 K. As Co_3O_4 is known to decompose to CoO at 1143 K [54], we propose that the initial product in the flame is the more stable CoO and it is oxidized only in the thin zone near the stagnation surface where flame temperature decreases sharply. The particle residence time in this zone is extremely short, and the oxidation reaction could be quenched by the cold stagnation surface before complete conversion to Co_3O_4.

The sub-stoichiometric Co^{3+} content is also consistent with the XRD results which indicate a lattice constant of $a = 8.10$-8.12 Å for the flame-synthesized Co_3O_4 nanoparticles (**Table S1**) in contrast to $a = 8.08$ Å for bulk Co_3O_4; the lattice expansion may be related to decreased ionic bonding within the crystal structure due to lack of the highly charged Co^{3+}.

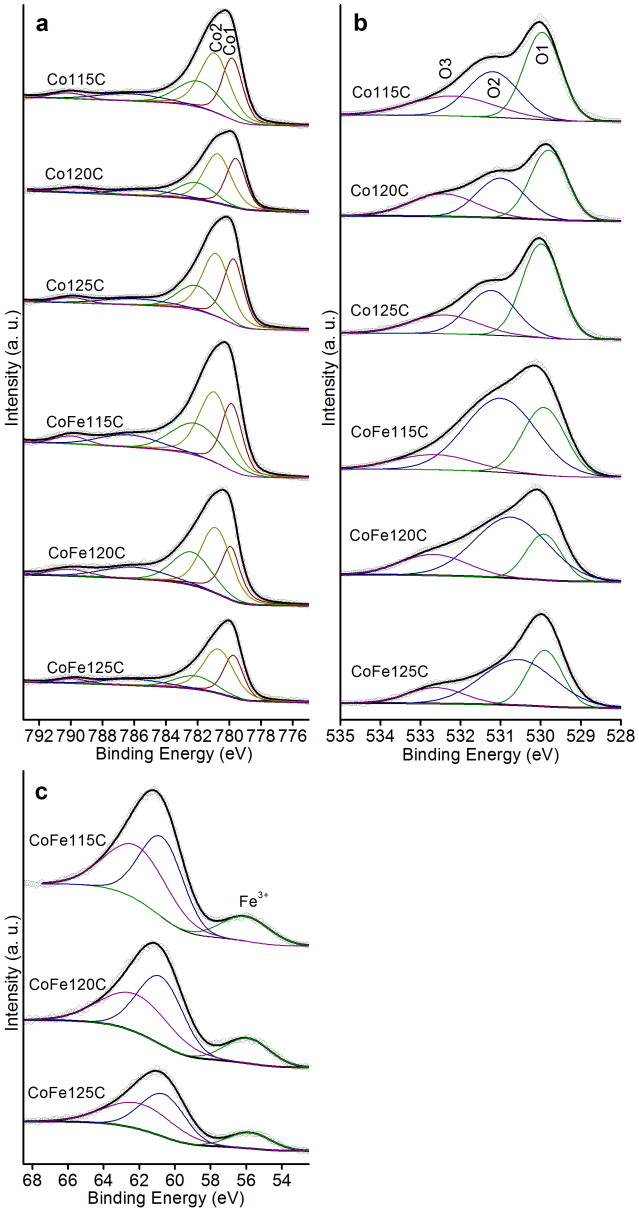

Figure 5: *X-ray photoelectron spectra in the (a) Co $2p_{3/2}$, (b) O 1s, and (c) Fe/Co 3p regions of the free-standing pure/Fe-doped Co_3O_4 powders.*

Figure 5b shows the O 2*s* spectra where 3 chemical states can be identified in general (also see **Table S5**). The peak at the binding energy of 529.9±0.1 eV (O1) is the signal of lattice oxygen in transition metal oxides, and the one at 532.4±0.2 eV (O3) is attributed to adsorbed water [5]. Assignment of the peak at the binding energy of 530.9±0.3 eV (O2) is more complicated, as signals in the same region have been associated with different

chemical species including metal hydroxides and defective metal oxides with oxygen vacancies [5]. In reported works on OER catalysts, high concentration of oxygen vacancies in spinel-type materials has been cited as an important factor in performance enhancement and has thus been intentionally generated [11, 66]. On the other hand, a recent in operando XPS study has found $Co(OH)_2$ on the surface of Co_3O_4 to be a promoting factor in the transformation into the CoO(OH) active phase [15], which is supported by the general observation that Co-based layered hydroxide materials have better OER performance than their spinel-type counterparts. Considering the high-temperature, humid environment in flame synthesis, both oxygen vacancies and hydroxide species may be present on the flame-synthesized nanoparticles. While it is difficult to distinguish between the two in this work, associating the O2 species with OER activity is nevertheless reasonable. As summarized in **Table 1**, the percentage of the O2 species remains relatively unchanged with different sublimator temperatures and increases significantly upon doping with Fe. It matches the trend in Tafel slope of the catalysts, confirming the promoting role of Fe.

3.2 Nanostructured Co_3O_4 and $Fe_xCo_{3-x}O_4$ Films

To demonstrate the potential of flame synthesis in electrode manufacture, 5×5 mm test electrodes were prepared by in situ deposition of Co_3O_4 and $Fe_xCo_{3-x}O_4$ films on graphite sheets (**Figure S3**). Graphite substrates fixed on the stagnation plate were directly impinged by the same particle-laden flames used to synthesize the free nanoparticles. In **Figure 6a**, the XRD patterns of the electrodes after 5 min of deposition confirm successful synthesis of spinel-type films. The relative intensities of the diffraction signals match the powder pattern of the reference Co_3O_4 spinel, indicating that the films do not have a preferential direction of crystal growth. As in the case of the free nanoparticles, doping with Fe leads to formation of a single-phase $Fe_xCo_{3-x}O_4$ solid solution with an expanded spinel lattice. The chemical composition of the films is consistent with that of the free particles, and catalyst loading increases with sublimator temperature (**Table S6**). However, **Table 2** shows an opposite trend in crystallite size of the flame-synthesized films compared with the free particles. The more visual results from SEM characterization presented in **Figure 6b-i** corroborate the XRD findings. Moreover, for both the Co_3O_4 and $Fe_xCo_{3-x}O_4$ a dramatic change in film morphology from columnar to granular, cauliflower-like can be observed with the increase in sublimator temperature. Similar morphological changes have been found in a few pioneering works on flame-synthesized ZnO, SnO_2 and TiO_2 films [41, 48, 49, 64]. As proposed by Thimsen and Biswas [48], the morphology of the films is determined by the relative speed of particle accumulation and sintering on substrate. Sintering is accelerated by small particle size and high temperature, resulting in columnar or denser films if its rate exceeds that of particle deposition [48]. In the present work the substrate temperature (570 °C) is not varied, and the size of the particles arriving at the substrate surface plays the major role in morphological control. We have shown by XRD analysis that the size of the Co_3O_4 and $Fe_xCo_{3-x}O_4$ nanoparticles increases with sublimator temperature (**Table 1**), which according to the above mechanism is consistent with the decrease in crystallite size of the films. At the sublimator temperature of 120 °C, a hierarchical film morphology consisting of elongated nanoparticles organized in a branched structure is obtained (**Figure 6c,g**). It is apparently a manifestation of incomplete sintering of the nanoparticles arriving at the surface. In other words, the particle deposition and

sintering probably occur in similar time scales during the synthesis of Co120C5min and CoFe120C5min. In addition, the crystallite sizes of all the film samples are significantly larger than those of the free nanoparticles, confirming that sintering does play an important role during film formation. In contrast, sintering is less important in the synthesis of the free nanoparticles because the particles are effectively cooled by the stagnation plate which is kept at 150 °C.

Table 2: *OER performance of pure/Fe-doped Co_3O_4 films deposited on graphite substrate*

Film	Crystallite size (nm)	η_{10} (mV)	Current density at $\eta = 400$ mV (mA/cm^2)	Mass activity at $\eta = 400$ mV (mA/mg)	Tafel slope (mV/dec)
Co115C5min	90	399	10.5	94	70
Co120C5min	17	379	21.1	206	61
Co125C5min	12	377	25.1	93	57
CoFe115C5min	38	386	17.2	138	55
CoFe120C5min	13	374	30.6	209	53
CoFe125C5min	10	364	47.3	145	50

The flame-synthesized Co_3O_4 and $Fe_xCo_{3-x}O_4$ films have sufficient mechanical strength to serve as working electrodes in OER without further treatment. The LSV curves presented in **Figure 7** show a rather flat pre-OER region for all the six films; the anodic Co(III)/Co(IV) wave is only observed for Co120C5min and Co125C5min films with similar intensities which are about 50 times lower than those for the Co_3O_4 nanoparticles. For Co115C5min, no such wave can be resolved. As Co(IV) species formed in situ are necessary to OER activity in Co_3O_4-based catalysts [15, 16], the different intensities of Co(III)/Co(IV) wave can be related to the OER performance of the Co_3O_4 films summarized in **Table 2**. Indeed, the overpotentials of Co120C5min and Co125C5min are similar and lower than that of Co115C5min. The difference between Co115C5min and Co120C5min can be attributed to more exposed active sites provided by the smaller film crystallite size and higher film porosity at higher sublimator temperatures. On the other hand, the same factors do not explain the remarkably higher mass activity of Co120C5min than Co125C5min (**Table 2**), because the larger crystallite size and denser structure of the former predict a smaller specific surface area which would lead to lower mass activity with other conditions unchanged. We ascribe the high mass activity of Co120C5min to its unique hierarchical structure; compared with the small spherical particles in Co125C5min, the elongated primary particles in Co120C5min introduce fewer grain boundaries along the electrical pathway and hence facilitate more efficient electron transport, which may provide better access to active sites [49]. The OER activity of the Fe-doped films follows a similar trend as in the pure Co_3O_4 films, and can be explained by the same factors. In general the OER kinetics is improved by the Fe dopant as reflected by the lower Tafel slopes of $Fe_xCo_{3-x}O_4$ films, which allows for better OER performance. Optimal mass activity of the $Fe_xCo_{3-x}O_4$ films is also found with the hierarchically structured CoFe120C5min, confirming the advantage of such morphology. Finally, it has to be pointed out that the films have lower activity compared with the Co_3O_4 and $Fe_xCo_{3-x}O_4$ powders supported on Ni foam, most probably due to low electrical conductivity of the films and loss of active surface during sintering. We are currently carrying out further studies to control the particle sintering and optimize the electrical contact between the catalyst and substrate.

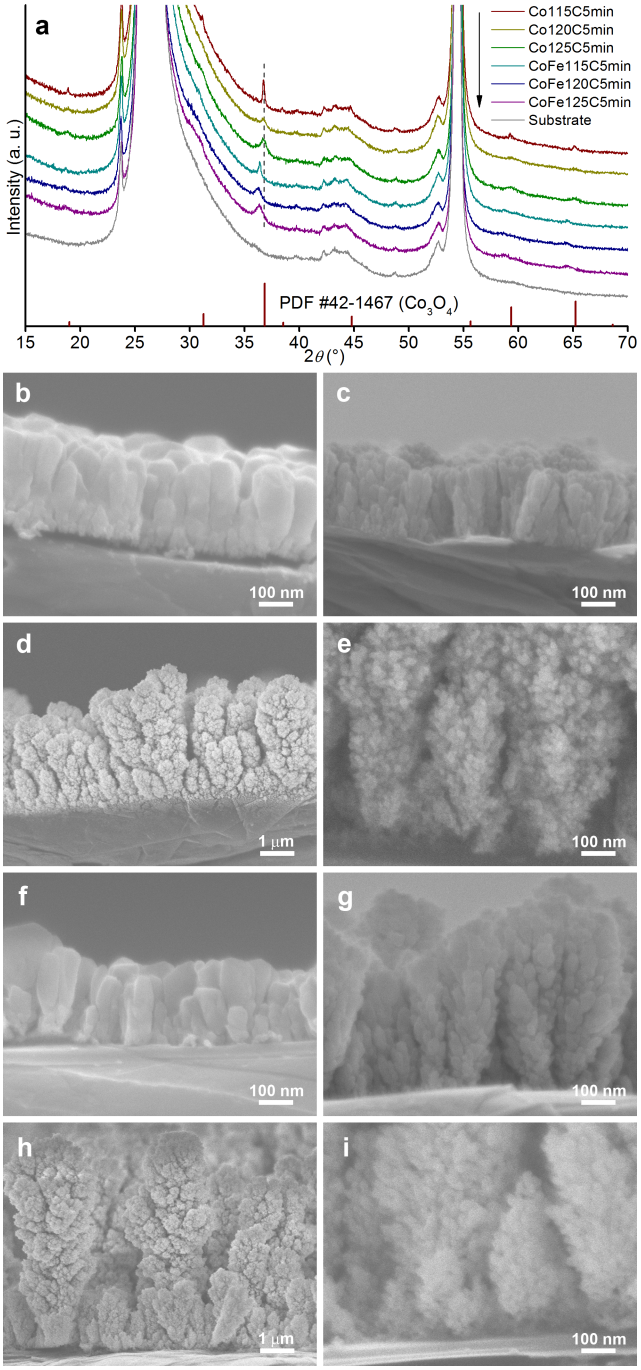

Figure 6: *(a) XRD patterns of the graphite electrodes coated with Co_3O_4 and $Fe_xCo_{3-x}O_4$. An XRD pattern of clean substrate is also shown for comparison. (b-i) SEM images of cross-sections of (b) Co115C5min, (c) Co120C5min, (d, e) Co125C5min, (f) CoFe115C5min, (g) CoFe120C5min, and (h, i) CoFe125C5min films.*

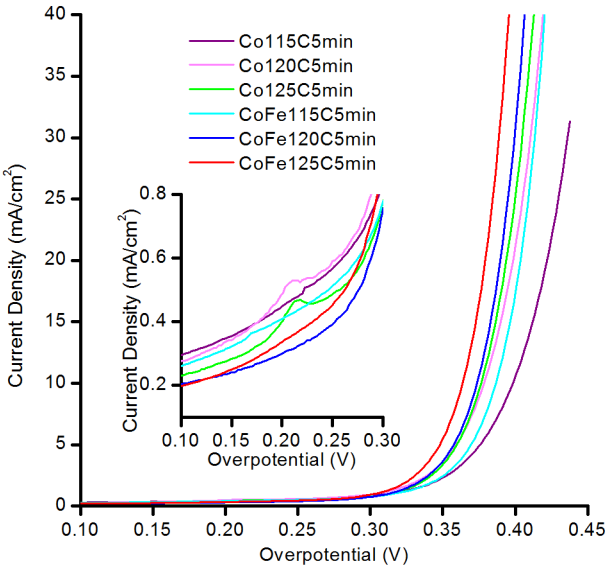

Figure 7: *LSV curves from OER tests on the Co_3O_4 and $Fe_xCo_{3-x}O_4$ films deposited on graphite substrate. Inset: magnified view of the pre-OER region.*

4 Conclusion

We demonstrated the application of vapor-fed flame aerosol synthesis (VFAS) in the production of nanoparticulate Co_3O_4 and $Fe_xCo_{3-x}O_4$ OER catalysts for the first time. Due to the short residence time and fast quenching in the premixed stagnation flame, the nanoparticle products have ultrasmall sizes, narrow size distributions and abundant surface defects which lead to low OER overpotential and Tafel slope with highly stable performance comparable to some of the best Co_3O_4-based catalysts synthesized by wet chemical methods. Moreover, nanostructured Co_3O_4 and $Fe_xCo_{3-x}O_4$ thin films were successfully grown on graphite substrates using VFAS and served as fully functional OER electrodes without further treatment. The morphology of the films was tuned facilely from dense columnar to porous granular, achieving the most efficient utilization of catalytic materials with the intermediate morphology consisting of hierarchically ordered elongated particles. In addition, the OER performance of both the nanoparticles and the films was improved by introducing the Fe dopant. This work expands the scope of the VFAS technique, proves it to be a valuable tool in the design and production of highly active OER catalysts, and highlights its potential for practical use as a sustainable technology in the energy industry.

5 Acknowledgments

The authors acknowledge the financial support of the Singapore National Research Foundation (NRF) through the Campus for Research Excellence and Technological Enterprise (CREATE) program.

A Supplementary Information

Experimental Details

Co_3O_4 and $Fe_xCo_{3-x}O_4$ were synthesized in a flame aerosol reactor at atmospheric pressure. It consists of an aerodynamically shaped nozzle with an exit diameter of 1.4 cm. The nozzle is heated electrically and kept at 180 °C. A gas mixture of $C_2H_4/O_2/Ar$ flows vertically downward to form a laminar jet at the exit and impinges on a water-cooled 3 cm thick aluminum stagnation plate placed 1.5 cm below the exit. The jet has a total flow rate of 18 L/min (STP) consisting of 3.4% of C_2H_4, 41.6% of O_2 and 55% of Ar (equivalence ratio $\phi = 0.25$). An annular flow of N_2 at 7 L/min (STP) surrounds the jet to separate it from the atmosphere. Flow rates of the unburnt gases are controlled individually by mass flow controllers. Upon ignition, a flat flame with a diameter of $\sim$2.5 cm is established above the surface of the stagnation plate. At steady state, the surface temperature of the stagnation plate is 150 °C as measured by a K-type thermocouple.

To introduce Fe and Co precursors into the flame, an in-house sublimator is connected in the Ar line. The sublimator consists of a stainless steel tube (1 cm I.D. by 11 cm length) packed with 1 g of $Co(acac)_2$ for synthesis of Co_3O_4 or a mixture of 1 g of $Co(acac)_2$ and 1 g of $Fe(acac)_3$ for synthesis of $Fe_xCo_{3-x}O_4$. The precursor is diluted by 11 g of 40 mesh α-Al_2O_3 (Kramer Industries) and the packed bed is held in the sublimator by glass wool at both ends. The sublimator is heated externally by 7 turns of glass insulated heater rope (FGR-100-240V, Omega Engineering), with the temperature monitored by a K-type thermocouple fixed at the middle of the exterior of the sublimator and controlled by a PID controller. During operation, the Ar was preheated by an inline gas heater to reach 90 °C before passing through the sublimator which was held at 115, 120, or 125 °C. The tubing connecting the sublimator and the nozzle is kept at 140-180 °C, and all the heated parts are insulated with woven fiberglass tape.

To synthesize free-standing Co_3O_4 and $Fe_xCo_{3-x}O_4$ powders, the burner was run with a precursor-loaded flame for 30 min as product accumulated on the stagnation plate. After the burner was switched off, the stagnation plate was cooled down in laboratory air and the product was scraped off the plate.

To prepare Co_3O_4 and $Fe_xCo_{3-x}O_4$ films, 5×30 mm rectangular substrates were first made from a natural graphite sheet (0.5 mm thick, >99.5%, Latech Scientific Supply), cleaned by wiping with EtOH, and dried in air at 60 °C. A piece of such substrate was then placed under the middle of a precursor-loaded flame for 5 min, during which a good contact between the substrate and the stagnation plate was maintained. After the deposition, the substrate was withdrawn from the flame and cooled in laboratory air. The surface temperature of the substrate was measured by an S-type thermocouple (wire diameter = 75 μm) to be 570 °C in a clean flame.

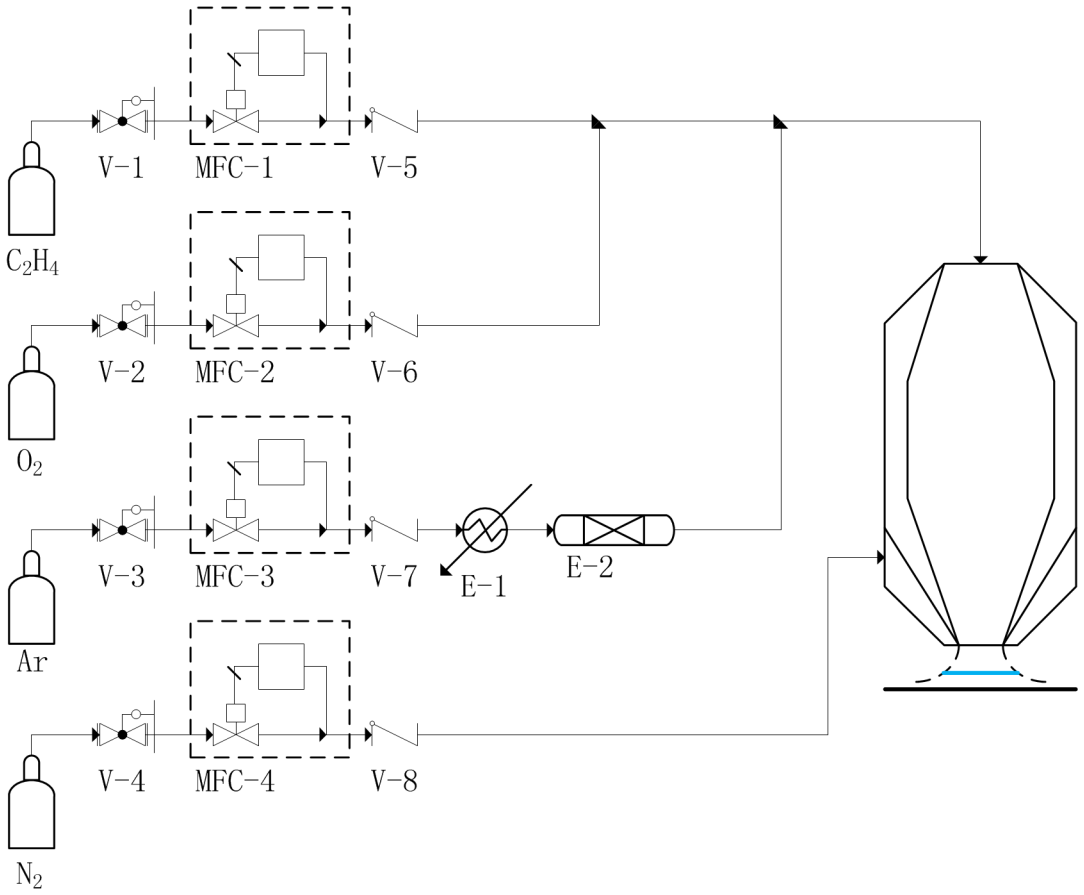

Figure S1: *Schematic diagram of the burner set-up. V-1 - V-4: pressure regulators, MFC-1 - MFC-4: mass flow controllers, V-5 - V-8: check valves, E-1: electrical inline gas heater, E-2: precursor sublimator.*

Table S1: *Crystallographic data derived from the XRD patterns of flame-synthesized Co_3O_4 and $Fe_xCo_{3-x}O_4$ powders.*

Sample	Lattice constant *a* (Å)	Crystallite size (nm) calculated from FWHM data of XRD peaks with Miller indexes:				
		(220)	(311)	(400)	(511)	(440)
Co115C	8.11	3.7	3.9	4.1	3.5	4.4
Co120C	8.12	4.8	4.8	4.0	4.4	4.8
Co125C	8.10	5.3	5.0	4.9	5.4	4.9
CoFe115C	8.18	3.8	3.8	3.8	3.6	3.5
CoFe120C	8.18	4.8	4.3	4.0	4.2	4.5
CoFe125C	8.16	5.8	5.4	4.7	5.3	5.4

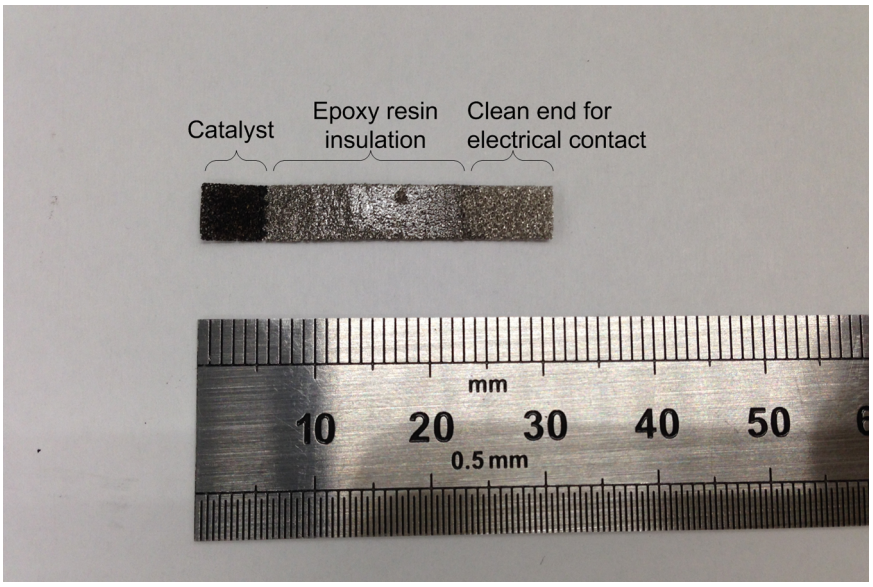

Figure S2: *Photograph of a Ni foam electrode loaded with flame-synthesized Co_3O_4 nanoparticles for electrochemical measurement.*

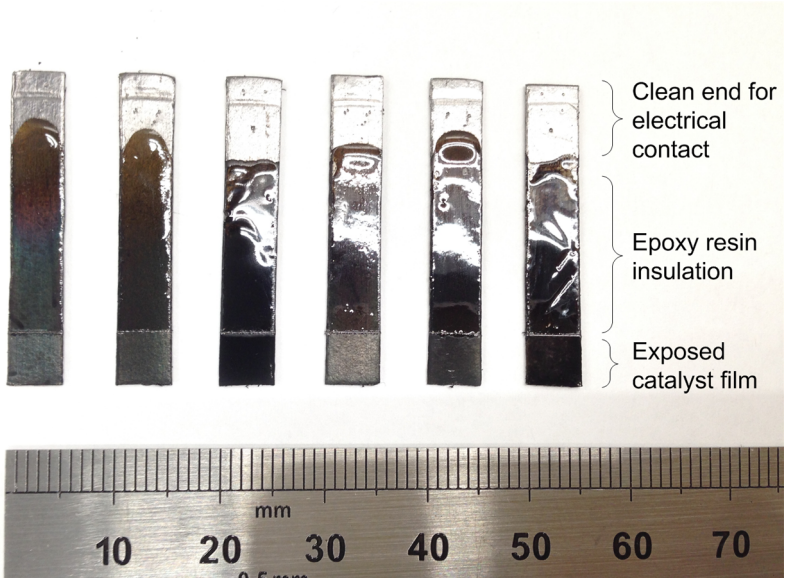

Figure S3: *Photograph of graphite electrodes with flame-grown pure/Fe-doped Co_3O_4 films for electrochemical measurement. From left to right: Co115C5min, Co120C5min, Co125C5min, CoFe115C5min, CoFe120C5min, and CoFe125C5min. The back side of the electrodes is also insulated by epoxy resin.*

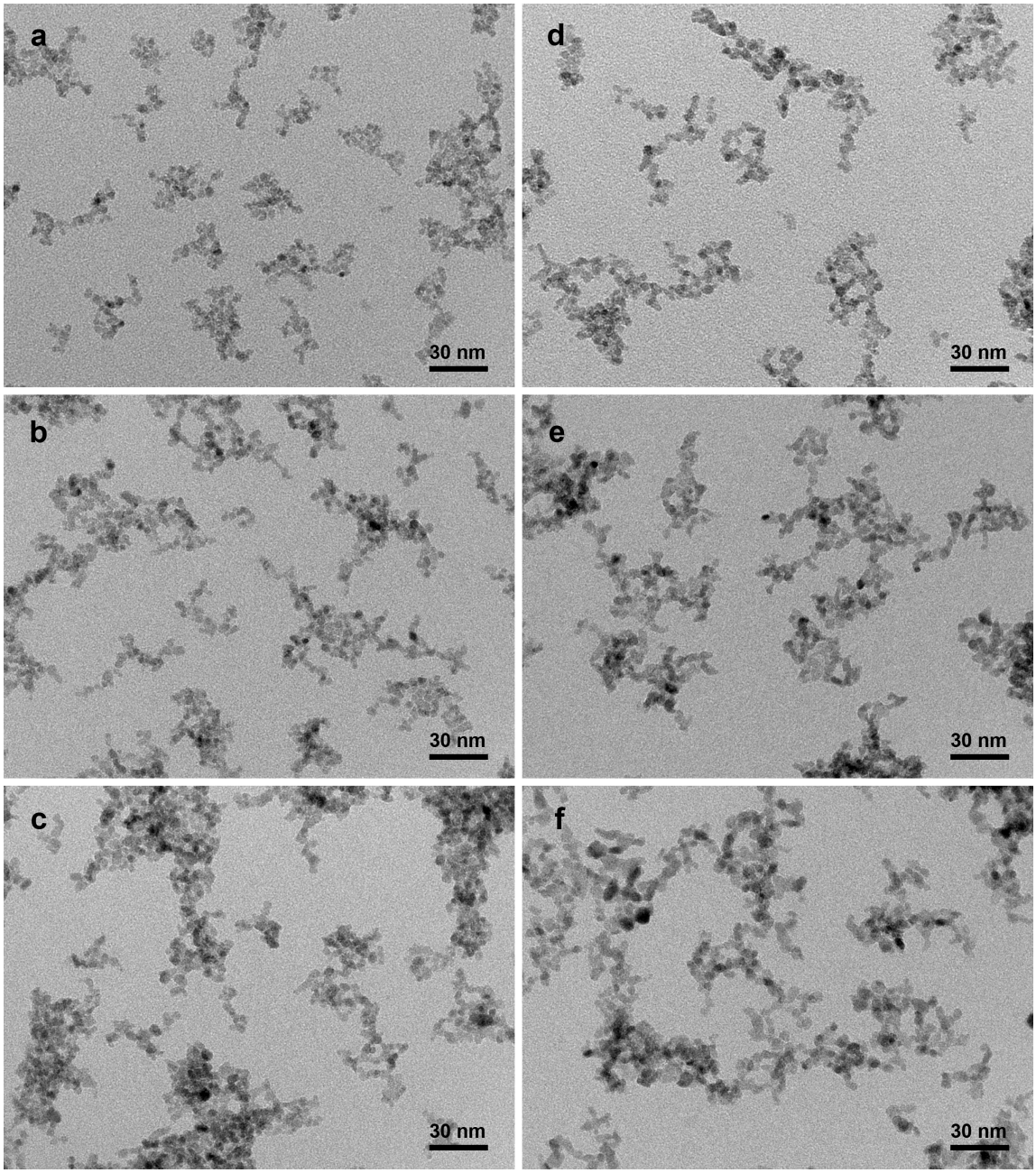

Figure S4: *TEM images of (a) Co115C, (b) Co120C, (c) Co125C, (d) CoFe115C, (e) CoFe120C, and (f) CoFe125C at low magnification.*

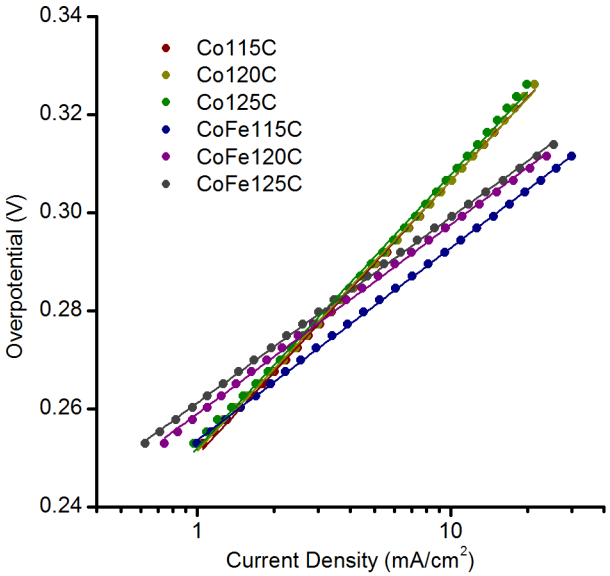

Figure S5: *Tafel plots fitted with the Tafel equation for the free-standing Co_3O_4 and $Fe_xCo_{3-x}O_4$ nanoparticles tested on Ni foam electrodes in 1M KOH.*

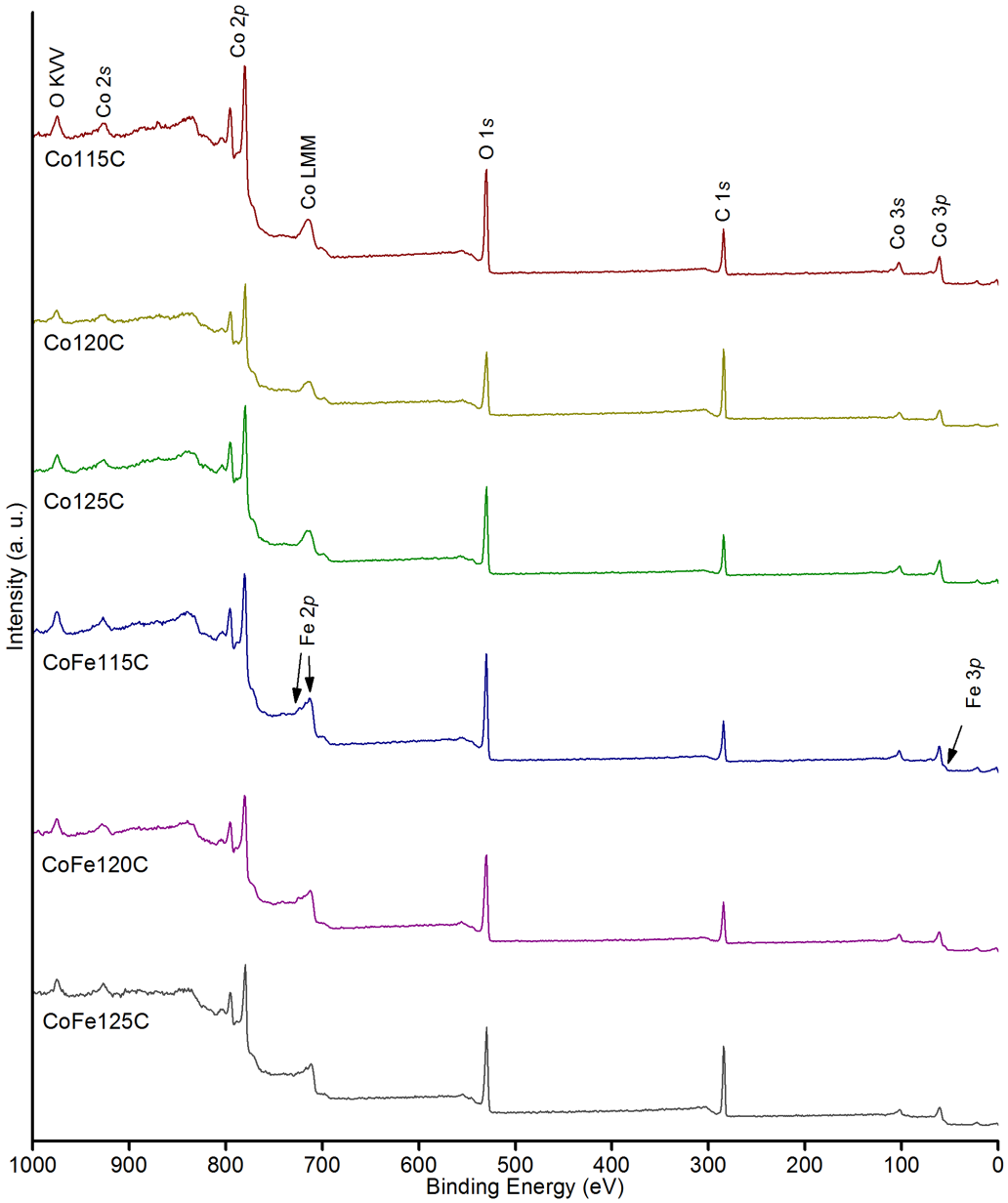

Figure S6: *XPS survey spectra of flame-synthesized Co_3O_4 and $Fe_xCo_{3-x}O_4$ powders.*

Table S2: *Reported OER performance of various spinel-type Co oxides and Fe-Co oxides.*

Catalyst	Synthesis method	Electrode material	Loading (mg/cm^2)	Electrolyte	η_{10} (mV)	Tafel slope (mV/dec)	Stability	Ref
Co_3O_4 NPs	Vapor-fed flame aerosol synthesis	Ni foam	1	1M KOH	299	55	N.A.	This work
Co_3O_4 NPs	Forced hydrolysis	Ni foam	1	1M KOH	328	N.A.	N.A.	[14]
Co_3O_4/N-rGO	Forced hydrolysis	Ni foam	1	1M KOH	310	67	13 mV increase in η_{10} with 1500 CV scans, 0.10 mg/cm^2 on GC	[29]
Holey Co_3O_4 nanosheets	Forced hydrolysis	GC	0.1	0.1M KOH	450	66	2% reduction in current at 0.9 V (Hg/HgO/0.1M KOH) with 2000 CV scans	[13]
Defective Co_3O_4 nanosheets	Ar plasma engraving	Ti foil	0.5	0.1M KOH	301	68	~8 mV increase in η_{10} with 2000 CV cycles	[60]
Co/Co_3O_4/N-C	Pyrolysis of ZIF-67	GC	0.4	1M KOH	391	103	3 mV increase in η_{10} with 3000 CV cycles	[3]
Co_3O_4/rGO composite nanosheets	Forced hydrolysis	CFP	0.2	1M KOH	290	68	0.5 mA/cm^2 decrease in current density with 10 h operation at ~12 mA/cm^2	[10]
Co_3O_4 nanorods	Anodization	Co foil	2.2	1M KOH	275	N.A.	~8 mV increase in η_{100} with 300 h operation	[11]
C-Co/Co_3O_4 hollow spheres	Forced hydrolysis, pyrolysis	GC	0.4	1M KOH	352	80	N.A.	[19]
Co_3O_4/rGO	Forced hydrolysis, post-synthesis grafting	GP	0.15	1M KOH	346	47	1 mV increase in η_{10} with 2 h operation	[25]
$Co_3O_{4-\delta}$ quantum dots	Repeated lithiation-delithiation of Co_3O_4	CFP	0.25	1M KOH	270	39	No decay in 30 h operation at $\eta = 290$ mV	[65]
Co_3O_4 NPs @ Co_3O_4 nanorods	Grafting of Co_3O_4 nanorods with ZIF-67, pyrolysis	Ni foil	0.88	1M KOH	301	115	54 mV increase in η_{10} with 10 h operation	[71]
C-Co_3O_4 NPs @ Co_3O_4 nanorods	Grafting of Co_3O_4 nanorods with ZIF-67, pyrolysis	Ni foil	0.70	1M KOH	261	65	<2% increase in η_{10} with 10 h operation	[71]
Hollow Co_3O_4 microtube array	Electrochemical conversion of $CoHPO_4$ microarray	Ni foam	N.A.	1M KOH	360 (η_{150})	84	5.5% reduction in current with 12 h operation at $\eta =$ 400 mV	[74]
Fe-doped Co_3O_4 NPs	Vapor-fed flame aerosol synthesis	Ni foam	1	1M KOH	295	39	<1 mV increase in η_{10} with 200 min operation	This work
Ordered mesoporous Fe-doped Co_3O_4	SiO_2-templated nanocasting	GC	0.12	0.1M KOH	486	N.A.	N.A.	[17]
Ordered mesoporous Fe-doped Co_3O_4	SiO_2-templated nanocasting	GC	N.A.	1M KOH	380	60	No decay in 33 h operation at $\eta = 440$ mV	[59]
$CoFe_2O_4$ NPs	Forced hydrolysis	CFP	1.03	1M NaOH	378	73	Nodecay in 40 h operation at ~10 mA/cm^2	[21]
$CoFe_2O_4$ nanofibers	Electrospinning	GC	0.42	0.1M KOH	410 (η_5)	82	8% reduction in current with 5.5 h operation at $\eta =$ 570 mV	[26]
$CoFe_2O_4$ hollow spheres	Forced hydrolysis on sacrificial carbon template	GC	0.4	0.1M KOH	450	N.A.	7.4% reduction in current with 12 h operation at $\eta =$ 530 mV	[61]
$CoFe_2O_4$/PANI-MWCNT	Surface grafting by forced hydrolysis	GC	0.285	1M KOH	314	31	~10% reduction in current with 40 h operation at ~9.5 mA/cm^2	[31]
$CoFe_2O_4$/NS-rGO	Forced hydrolysis	GC	0.8	0.1M KOH	635 (η_{23})	N.A.	24% reduction in current with 12 h operation at $\eta =$ 435 mV	[63]
C-$CoFe_2O_4$ nanorods	Surface grafting with MOF-74-Co/Fe, pyrolysis	Ni foam	1.03	1M KOH	240	45	0.4% increase in η_{10} with 30 h operation	[32]

NPs: nanoparticles; N-rGO: N-doped reduced graphene oxide; N-C: N-doped carbon; PANI-MWCNT: polyaniline-functionalized multi-wall carbon nanotube; NS-rGO: N, S co-doped reduced graphene oxide; GC: glassy carbon; CFP: carbon fiber paper; GP: graphite paper; η_{xx}: overpotential at current density of xx mA/cm^2

Table S3: *Deconvolution results of Co 2p XPS spectra of the flame-synthesized nanoparticles.*

Sample	Peak 1 B.E. (eV)	Peak 1 FWHM	Peak 2 B.E. (eV)	Peak 2 FWHM	Peak 3 B.E. (eV)	Peak 3 FWHM	Peak 4 B.E. (eV)	Peak 4 FWHM	Peak 5 B.E. (eV)	Peak 5 FWHM
Co115C	779.8	1.53	780.9	2.21	781.9	3.29	786.3	4.83	790.1	2.50
Co120C	779.6	1.45	780.8	2.04	782.1	2.62	785.3	4.49	789.6	2.87
Co125C	779.8	1.51	780.8	2.09	782.1	2.73	786.0	4.90	790.0	2.33
CoFe115C	779.9	1.53	781.0	2.31	782.1	3.75	786.3	4.45	790.0	2.36
CoFe120C	779.9	1.47	780.9	2.26	782.4	2.90	786.0	4.63	790.1	2.87
CoFe125C	779.8	1.47	780.7	2.30	782.2	3.04	786.0	4.55	789.9	2.21

Table S4: *Deconvolution results of Co/Fe 3p XPS spectra of the flame-synthesized nanoparticles.*

Sample	Peak 1 B.E. (eV)	Peak 1 FWHM	Peak 2 B.E. (eV)	Peak 2 FWHM	Peak 3 B.E. (eV)	Peak 3 FWHM
CoFe115C	55.8	3.04	60.4	2.56	61.8	3.93
CoFe120C	55.7	2.80	60.5	2.71	61.8	4.44
CoFe125C	55.5	2.66	60.3	2.60	61.6	4.40

Table S5: *Deconvolution results of O 1s XPS spectra of the flame-synthesized nanoparticles.*

Sample	Peak 1 B.E. (eV)	Peak 1 FWHM	Peak 2 B.E. (eV)	Peak 2 FWHM	Peak 3 B.E. (eV)	Peak 3 FWHM
Co115C	530.0	1.09	531.2	1.51	532.2	2.42
Co120C	529.8	1.08	531.0	1.39	532.4	1.96
Co125C	530.0	1.12	531.2	1.40	532.4	2.00
CoFe115C	529.9	1.25	531.0	2.09	532.7	2.30
CoFe120C	529.9	1.03	530.7	2.13	532.7	1.96
CoFe125C	529.9	1.03	530.6	2.14	532.6	1.66

Table S6: *Metal loading of the flame-synthesized films determined by ICPOES.*

Film	Co loading (mg/cm^2)	Fe loading (mg/cm^2)	Co/Fe ratio (mol/mol)
Co115C5min	0.082	Not detected	∞
Co120C5min	0.075	Not detected	∞
Co125C5min	0.197	Not detected	∞
CoFe115C5min	0.077	0.014	5.2
CoFe120C5min	0.088	0.019	4.4
CoFe125C5min	0.194	0.045	4.1

References

[1] CMCL Innovations. *k*inetics®, 2016. URL http://www.cmclinnovations.com.

[2] J. A. Azurdia, A. McCrum, and R. M. Laine. Systematic synthesis of mixed-metal oxides in NiO-Co_3O_4, NiO-MoO_3, and NiO-CuO systems via liquid-feed flame spray pyrolysis. *J. Mater. Chem.*, 18(27):3249, 2008. ISSN 0959-9428 1364-5501. doi:10.1039/b801745j.

[3] C. Bai, S. Wei, D. Deng, X. Lin, M. Zheng, and Q. Dong. A nitrogen-doped nano carbon dodecahedron with Co@Co_3O_4 implants as a bi-functional electrocatalyst for efficient overall water splitting. *J. Mater. Chem. A*, 5(20):9533–9536, 2017. ISSN 2050-7488 2050-7496. doi:10.1039/c7ta01708a.

[4] J. Bao, X. Zhang, B. Fan, J. Zhang, M. Zhou, W. Yang, X. Hu, H. Wang, B. Pan, and Y. Xie. Ultrathin spinel-structured nanosheets rich in oxygen deficiencies for enhanced electrocatalytic water oxidation. *Angew. Chem., Int. Ed. Engl.*, 54(25):7399–7404, 2015. ISSN 1521-3773 (Electronic) 1433-7851 (Linking). doi:10.1002/anie.201502226. URL http://www.ncbi.nlm.nih.gov/pubmed/25951435.

[5] M. C. Biesinger, B. P. Payne, A. P. Grosvenor, L. W. M. Lau, A. R. Gerson, and R. S. C. Smart. Resolving surface chemical states in XPS analysis of first row transition metals, oxides and hydroxides: Cr, Mn, Fe, Co and Ni. *Appl. Surf. Sci.*, 257 (7):2717–2730, 2011. ISSN 01694332. doi:10.1016/j.apsusc.2010.10.051.

[6] C. O. Blattmann, A. T. Guntner, and S. E. Pratsinis. In situ monitoring of the deposition of flame-made chemoresistive gas-sensing films. *ACS Appl. Mater. Interfaces*, 9(28):23926–23933, 2017. ISSN 1944-8252 (Electronic) 1944-8244 (Linking). doi:10.1021/acsami.7b04530. URL http://www.ncbi.nlm.nih.gov/pubmed/28621930.

[7] M. S. Burke, M. G. Kast, L. Trotochaud, A. M. Smith, and S. W. Boettcher. Cobalt-iron (oxy)hydroxide oxygen evolution electrocatalysts: the role of structure and composition on activity, stability, and mechanism. *J. Am. Chem. Soc.*, 137(10):3638–3648, 2015. ISSN 1520-5126 (Electronic) 0002-7863 (Linking). doi:10.1021/jacs.5b00281. URL http://www.ncbi.nlm.nih.gov/pubmed/25700234.

[8] I. G. Casella and M. Gatta. Study of the electrochemical deposition and properties of cobalt oxide species in citrate alkaline solutions. *J. Electroanal. Chem.*, 534(1): 31–38, 2002. ISSN 15726657. doi:10.1016/s0022-0728(02)01100-2.

[9] L. Chen, X. Dong, Y. Wang, and Y. Xia. Separating hydrogen and oxygen evolution in alkaline water electrolysis using nickel hydroxide. *Nat. Commun.*, 7:11741, 2016. ISSN 2041-1723 (Electronic) 2041-1723 (Linking). doi:10.1038/ncomms11741. URL http://www.ncbi.nlm.nih.gov/pubmed/27199009.

[10] Y. Chen, J. Hu, H. Diao, W. Luo, and Y. F. Song. Facile preparation of ultrathin Co_3O_4/nanocarbon composites with greatly improved surface activity as a highly efficient oxygen evolution reaction catalyst. *Chem. - Eur. J.*, 23(16):4010–4016, 2017. ISSN 1521-3765 (Electronic) 0947-6539 (Linking). doi:10.1002/chem.201700225. URL http://www.ncbi.nlm.nih.gov/pubmed/28150913.

[11] G. Cheng, T. Kou, J. Zhang, C. Si, H. Gao, and Z. Zhang. O_2^{2-}/O^- functionalized oxygen-deficient Co_3O_4 nanorods as high performance supercapacitor electrodes and electrocatalysts towards water splitting. *Nano Energy*, 38:155–166, 2017. ISSN 22112855. doi:10.1016/j.nanoen.2017.05.043.

[12] X. Deng, S. Ozturk, C. Weidenthaler, and H. Tuysuz. Iron-induced activation of ordered mesoporous nickel cobalt oxide electrocatalyst for the oxygen evolution reaction. *ACS Appl. Mater. Interfaces*, 9(25):21225–21233, 2017. ISSN 1944-8252 (Electronic) 1944-8244 (Linking). doi:10.1021/acsami.7b02571. URL http://www.ncbi.nlm.nih.gov/pubmed/28582615.

[13] Y. Dou, T. Liao, Z. Ma, D. Tian, Q. Liu, F. Xiao, Z. Sun, J. Ho Kim, and S. Xue Dou. Graphene-like holey Co_3O_4 nanosheets as a highly efficient catalyst for oxygen evolution reaction. *Nano Energy*, 30:267–275, 2016. ISSN 22112855. doi:10.1016/j.nanoen.2016.10.020.

[14] A. J. Esswein, M. J. McMurdo, P. N. Ross, A. T. Bell, and T. D. Tilley. Size-dependent activity of Co_3O_4 nanoparticle anodes for alkaline water electrolysis. *J. Phys. Chem. C*, 113(33):15068–15072, 2009. ISSN 1932-7447 1932-7455. doi:10.1021/jp904022e.

[15] M. Favaro, J. Yang, S. Nappini, E. Magnano, F. M. Toma, E. J. Crumlin, J. Yano, and I. D. Sharp. Understanding the oxygen evolution reaction mechanism on CoO_x using operando ambient-pressure x-ray photoelectron spectroscopy. *J. Am. Chem. Soc.*, 139(26):8960–8970, 2017. ISSN 1520-5126 (Electronic) 0002-7863 (Linking). doi:10.1021/jacs.7b03211. URL http://www.ncbi.nlm.nih.gov/pubmed/28598604.

[16] J. B. Gerken, J. G. McAlpin, J. Y. Chen, M. L. Rigsby, W. H. Casey, R. D. Britt, and S. S. Stahl. Electrochemical water oxidation with cobalt-based electrocatalysts from pH 0-14: the thermodynamic basis for catalyst structure, stability, and activity. *J. Am. Chem. Soc.*, 133(36):14431–14442, 2011. ISSN 1520-5126 (Electronic) 0002-7863 (Linking). doi:10.1021/ja205647m. URL http://www.ncbi.nlm.nih.gov/pubmed/21806043.

[17] T. Grewe, X. Deng, and H. Tuysuz. Influence of fe doping on structure and water oxidation activity of nanocast Co_3O_4. *Chem. Mater.*, 26(10):3162–3168, 2014. ISSN 0897-4756 1520-5002. doi:10.1021/cm5005888.

[18] S. Han, S. Liu, R. Wang, X. Liu, L. Bai, and Z. He. One-step electrodeposition of nanocrystalline $Zn_xCo_{3-x}O_4$ films with high activity and stability for electrocatalytic oxygen evolution. *ACS Appl. Mater. Interfaces*, 9(20):17186–17194, 2017. ISSN 1944-8252 (Electronic) 1944-8244 (Linking). doi:10.1021/acsami.7b04841. URL http://www.ncbi.nlm.nih.gov/pubmed/28467838.

[19] L. Hang, Y. Sun, D. Men, S. Liu, Q. Zhao, W. Cai, and Y. Li. Hierarchical micro/nanostructured C doped Co/Co_3O_4 hollow spheres derived from PS@$Co(OH)_2$ for the oxygen evolution reaction. *J. Mater. Chem. A*, 5(22):11163–11170, 2017. ISSN 2050-7488 2050-7496. doi:10.1039/c7ta02539d.

[20] Y. Jiao, Y. Zheng, M. Jaroniec, and S. Z. Qiao. Design of electrocatalysts for oxygen- and hydrogen-involving energy conversion reactions. *Chem. Soc. Rev.*, 44(8):2060–2086, 2015. ISSN 1460-4744 (Electronic) 0306-0012 (Linking). doi:10.1039/c4cs00470a. URL http://www.ncbi.nlm.nih.gov/pubmed/25672249.

[21] A. Kargar, S. Yavuz, T. K. Kim, C. H. Liu, C. Kuru, C. S. Rustomji, S. Jin, and P. R. Bandaru. Solution-processed $CoFe_2O_4$ nanoparticles on 3D carbon fiber papers for durable oxygen evolution reaction. *ACS Appl. Mater. Interfaces*, 7(32):17851–17856, 2015. ISSN 1944-8252 (Electronic) 1944-8244 (Linking). doi:10.1021/acsami.5b04270. URL http://www.ncbi.nlm.nih.gov/pubmed/26217939.

[22] Y. Kim, Y. Yoon, and D. Shin. Charge-discharge characteristics of nanocrystalline Co_3O_4 powders via aerosol flame synthesis. *Solid State Ionics*, 192(1):308–312, 2011. ISSN 01672738. doi:10.1016/j.ssi.2010.06.021.

[23] R. Koirala, S. E. Pratsinis, and A. Baiker. Synthesis of catalytic materials in flames: opportunities and challenges. *Chem. Soc. Rev.*, 45(11):3053–3068, 2016. ISSN 1460-4744 (Electronic) 0306-0012 (Linking). doi:10.1039/c5cs00011d. URL http://www.ncbi.nlm.nih.gov/pubmed/27108487.

[24] Y. Lee, J. Suntivich, K. J. May, E. E. Perry, and Y. Shao-Horn. Synthesis and activities of rutile IrO_2 and RuO_2 nanoparticles for oxygen evolution in acid and alkaline solutions. *J. Phys. Chem. Lett.*, 3(3):399–404, 2012. ISSN 1948-7185 (Print) 1948-7185 (Linking). doi:10.1021/jz2016507. URL http://www.ncbi.nlm.nih.gov/pubmed/26285858.

[25] M. Leng, X. Huang, W. Xiao, J. Ding, B. Liu, Y. Du, and J. Xue. Enhanced oxygen evolution reaction by Co-O-C bonds in rationally designed Co_3O_4 /graphene nanocomposites. *Nano Energy*, 33:445–452, 2017. ISSN 22112855. doi:10.1016/j.nanoen.2017.01.061.

[26] M. Li, Y. Xiong, X. Liu, X. Bo, Y. Zhang, C. Han, and L. Guo. Facile synthesis of electrospun MFe_2O_4 (M = Co, Ni, Cu, Mn) spinel nanofibers with excellent electrocatalytic properties for oxygen evolution and hydrogen peroxide reduction. *Nanoscale*, 7(19):8920–8930, 2015. ISSN 2040-3372 (Electronic) 2040-3364 (Linking). doi:10.1039/c4nr07243j. URL http://www.ncbi.nlm.nih.gov/pubmed/25917286.

[27] S. Li, Y. Ren, P. Biswas, and S. D. Tse. Flame aerosol synthesis of nanostructured materials and functional devices: Processing, modeling, and diagnostics. *Prog. Energy Combust. Sci.*, 55:1–59, 2016. ISSN 03601285. doi:10.1016/j.pecs.2016.04.002.

[28] Y. Li, Y. Hu, J. Huo, H. Jiang, C. Li, and G. Huang. Stable core shell Co_3Fe_7-$CoFe_2O_4$ nanoparticles synthesized via flame spray pyrolysis approach. *Ind. Eng. Chem. Res.*, 51(34):11157–11162, 2012. ISSN 0888-5885 1520-5045. doi:10.1021/ie3010644.

[29] Y. Liang, Y. Li, H. Wang, J. Zhou, J. Wang, T. Regier, and H. Dai. Co_3O_4 nanocrystals on graphene as a synergistic catalyst for oxygen reduction reaction. *Nat. Mater.*, 10(10):780–786, 2011. ISSN 1476-1122 (Print) 1476-1122 (Linking). doi:10.1038/nmat3087. URL http://www.ncbi.nlm.nih.gov/pubmed/21822263.

[30] Y. Liu, S. Zha, and M. Liu. Novel nanostructured electrodes for solid oxide fuel cells fabricated by combustion chemical vapor deposition (CVD). *Adv. Mater.*, 16 (3):256–260, 2004. ISSN 0935-9648 1521-4095. doi:10.1002/adma.200305767.

[31] Y. Liu, J. Li, F. Li, W. Li, H. Yang, X. Zhang, Y. Liu, and J. Ma. A facile preparation of $CoFe_2O_4$ nanoparticles on polyaniline-functionalised carbon nanotubes as enhanced catalysts for the oxygen evolution reaction. *J. Mater. Chem. A*, 4(12): 4472–4478, 2016. ISSN 2050-7488 2050-7496. doi:10.1039/c5ta10420c.

[32] X. F. Lu, L. F. Gu, J. W. Wang, J. X. Wu, P. Q. Liao, and G. R. Li. Bimetal-organic framework derived $CoFe_2O_4$/C porous hybrid nanorod arrays as high-performance electrocatalysts for oxygen evolution reaction. *Adv. Mater.*, 29(3):1604437, 2017. ISSN 1521-4095 (Electronic) 0935-9648 (Linking). doi:10.1002/adma.201604437. URL http://www.ncbi.nlm.nih.gov/pubmed/27865016.

[33] M. Y. Manuputty, J. Akroyd, S. Mosbach, and M. Kraft. Modelling TiO_2 formation in a stagnation flame using method of moments with interpolative closure. *Combust. Flame*, 178(Supplement C):135 – 147, 2017. ISSN 0010-2180. doi:https://doi.org/10.1016/j.combustflame.2017.01.005. URL http://www.sciencedirect.com/science/article/pii/S0010218017300056.

[34] N. S. McIntyre and D. G. Zetaruk. X-ray photoelectron spectroscopic studies of iron oxides. *Anal. Chem.*, 49(11):1521–1529, 1977. ISSN 0003-2700 1520-6882. doi:10.1021/ac50019a016.

[35] P. W. Menezes, A. Indra, A. Bergmann, P. Chernev, C. Walter, H. Dau, P. Strasser, and M. Driess. Uncovering the prominent role of metal ions in octahedral versus tetrahedral sites of cobalt-zinc oxide catalysts for efficient oxidation of water. *J. Mater. Chem. A*, 4(25):10014–10022, 2016. ISSN 2050-7488 2050-7496. doi:10.1039/c6ta03644a.

[36] W. Merchan-Merchan, A. V. Saveliev, L. Kennedy, and W. C. Jimenez. Combustion synthesis of carbon nanotubes and related nanostructures. *Prog. Energy Combust. Sci.*, 36(6):696–727, 2010. ISSN 03601285. doi:10.1016/j.pecs.2010.02.005.

[37] J. H. Montoya, L. C. Seitz, P. Chakthranont, A. Vojvodic, T. F. Jaramillo, and J. K. Norskov. Materials for solar fuels and chemicals. *Nat. Mater.*, 16(1):70–81, 2016. ISSN 1476-1122 (Print) 1476-1122 (Linking). doi:10.1038/nmat4778. URL http://www.ncbi.nlm.nih.gov/pubmed/27994241.

[38] C. G. Morales-Guio, L. Liardet, and X. Hu. Oxidatively electrodeposited thin-film transition metal (oxy)hydroxides as oxygen evolution catalysts. *J. Am. Chem. Soc.*, 138(28):8946–8957, 2016. ISSN 1520-5126 (Electronic) 0002-7863 (Linking). doi:10.1021/jacs.6b05196. URL http://www.ncbi.nlm.nih.gov/pubmed/27344954.

[39] R. Mueller, L. Madler, and S. E. Pratsinis. Nanoparticle synthesis at high production rates by flame spray pyrolysis. *Chem. Eng. Sci.*, 58(10):1969–1976, 2003. ISSN 00092509. doi:10.1016/s0009-2509(03)00022-8.

[40] S. Nikraz and H. Wang. Dye sensitized solar cells prepared by flames stabilized on a rotating surface. *Proc. Combust. Inst.*, 34(2):2171–2178, 2013. ISSN 15407489. doi:10.1016/j.proci.2012.06.069.

[41] T. A. Polley, W. B. Carter, and P. D, B. Deposition of zinc oxide thin films by combustion CVD. *Thin Solid Films*, 357(2):132–136, 1999.

[42] S. E. Pratsinis. Flame aerosol synthesis of ceramic powders. *Prog. Energy Combust. Sci.*, 24(3):197–219, 1998. ISSN 03601285. doi:10.1016/s0360-1285(97)00028-2.

[43] S. K. Singh, V. M. Dhavale, and S. Kurungot. Low surface energy plane exposed Co_3O_4 nanocubes supported on nitrogen-doped graphene as an electrocatalyst for efficient water oxidation. *ACS Appl. Mater. Interfaces*, 7(1):442–451, 2015. ISSN 1944-8252 (Electronic) 1944-8244 (Linking). doi:10.1021/am506450c. URL http://www.ncbi.nlm.nih.gov/pubmed/25495057.

[44] F. Song and X. Hu. Exfoliation of layered double hydroxides for enhanced oxygen evolution catalysis. *Nat. Commun.*, 5:4477, 2014. ISSN 2041-1723 (Electronic) 2041-1723 (Linking). doi:10.1038/ncomms5477. URL http://www.ncbi.nlm.nih.gov/pubmed/25030209.

[45] M. B. Stevens, L. J. Enman, A. S. Batchellor, M. R. Cosby, A. E. Vise, C. D. M. Trang, and S. W. Boettcher. Measurement techniques for the study of thin film heterogeneous water oxidation electrocatalysts. *Chem. Mater.*, 29(1):120–140, 2017. ISSN 0897-4756 1520-5002. doi:10.1021/acs.chemmater.6b02796.

[46] N. T. Suen, S. F. Hung, Q. Quan, N. Zhang, Y. J. Xu, and H. M. Chen. Electrocatalysis for the oxygen evolution reaction: recent development and future perspectives. *Chem. Soc. Rev.*, 46(2):337–365, 2017. ISSN 1460-4744 (Electronic) 0306-0012 (Linking). doi:10.1039/c6cs00328a. URL http://www.ncbi.nlm.nih.gov/pubmed/28083578.

[47] W. Y. Teoh, R. Setiawan, J.-D. Grunwaldt, R. Amal, and S. E. Pratsinis. Ru-doped cobalt-zirconia nanocomposites by flame synthesis: Physicochemical and catalytic properties. *Chem. Mater.*, 20(12):4069–4079, 2008. ISSN 0897-4756 1520-5002. doi:10.1021/cm8002657.

[48] E. Thimsen and P. Biswas. Nanostructured photoactive films synthesized by a flame aerosol reactor. *AIChE J.*, 53(7):1727–1735, 2007. ISSN 00011541 15475905. doi:10.1002/aic.11210.

[49] E. Thimsen, N. Rastgar, and P. Biswas. Nanostructured TiO_2 films with controlled morphology synthesized in a single step process: Performance of dye-sensitized solar cells and photo watersplitting. *J. Phys. Chem. C*, 112(11):4134–4140, 2008. ISSN 1932-7447 1932-7455. doi:10.1021/jp710422f.

[50] E. D. Tolmachoff, A. D. Abid, D. J. Phares, C. S. Campbell, and H. Wang. Synthesis of nano-phase TiO_2 crystalline films over premixed stagnation flames. *Proc. Combust. Inst.*, 32(2):1839–1845, 2009. ISSN 15407489. doi:10.1016/j.proci.2008.06.052.

[51] L. Trotochaud, S. L. Young, J. K. Ranney, and S. W. Boettcher. Nickel-iron oxyhydroxide oxygen-evolution electrocatalysts: the role of intentional and incidental iron incorporation. *J. Am. Chem. Soc.*, 136(18):6744–6753, 2014. ISSN 1520-5126 (Electronic) 0002-7863 (Linking). doi:10.1021/ja502379c. URL http://www.ncbi.nlm.nih.gov/pubmed/24779732.

[52] A. C. C. Tseung and S. Jasem. Oxygen evolution on semiconducting oxides. *Electrochim. Acta*, 22(1):31–34, 1977. ISSN 00134686. doi:10.1016/0013-4686(77)85049-4.

[53] M. G. Walter, E. L. Warren, J. R. McKone, S. W. Boettcher, Q. Mi, E. A. Santori, and N. S. Lewis. Solar water splitting cells. *Chem. Rev.*, 110(11):6446–6473, 2010. ISSN 1520-6890 (Electronic) 0009-2665 (Linking). doi:10.1021/cr1002326. URL http://www.ncbi.nlm.nih.gov/pubmed/21062097.

[54] C.-B. Wang, H.-K. Lin, and C.-W. Tang. Thermal characterization and microstructure change of cobalt oxides. *Catal. Lett.*, 94(1/2):69–74, 2004. ISSN 1011-372X. doi:10.1023/B:CATL.0000019333.73968.c6.

[55] H. Wang, X. You, A. V. Joshi, S. G. Davis, A. Laskin, F. Egolfopoulos, and C. K. Law. USC Mech Version II. high-temperature combustion reaction model of H_2/CO/C1-C4 compounds, May 2007 2007. URL http://ignis.usc.edu/USC_Mech_II.htm.

[56] H. Y. Wang, S. F. Hung, H. Y. Chen, T. S. Chan, H. M. Chen, and B. Liu. In operando identification of geometrical-site-dependent water oxidation activity of spinel Co_3O_4. *J. Am. Chem. Soc.*, 138(1):36–39, 2016. ISSN 1520-5126 (Electronic) 0002-7863 (Linking). doi:10.1021/jacs.5b10525. URL http://www.ncbi.nlm.nih.gov/pubmed/26710084.

[57] J. Wang, W. Cui, Q. Liu, Z. Xing, A. M. Asiri, and X. Sun. Recent progress in cobalt-based heterogeneous catalysts for electrochemical water splitting. *Adv. Mater.*, 28(2):215–230, 2016. ISSN 1521-4095 (Electronic) 0935-9648 (Linking). doi:10.1002/adma.201502696. URL http://www.ncbi.nlm.nih.gov/pubmed/26551487.

[58] B. Y. Xia, Y. Yan, N. Li, H. B. Wu, X. W. Lou, and X. Wang. A metal-organic framework-derived bifunctional oxygen electrocatalyst. *Nat. Energy*, 1(1):15006, 2016. ISSN 2058-7546. doi:10.1038/nenergy.2015.6.

[59] C. Xiao, X. Lu, and C. Zhao. Unusual synergistic effects upon incorporation of Fe and/or Ni into mesoporous Co_3O_4 for enhanced oxygen evolution. *Chem. Commun. (Cambridge, U. K.)*, 50(70):10122–10125, 2014. ISSN 1364-548X (Electronic) 1359-7345 (Linking). doi:10.1039/c4cc04922e. URL http://www.ncbi.nlm.nih.gov/pubmed/25050969.

[60] L. Xu, Q. Jiang, Z. Xiao, X. Li, J. Huo, S. Wang, and L. Dai. Plasma-engraved Co_3O_4 nanosheets with oxygen vacancies and high surface area for the oxygen evolution reaction. *Angew. Chem., Int. Ed. Engl.*, 55(17):5277–5281, 2016. ISSN 1521-3773 (Electronic) 1433-7851 (Linking). doi:10.1002/anie.201600687. URL http://www.ncbi.nlm.nih.gov/pubmed/26990905.

[61] Y. Xu, W. Bian, J. Wu, J.-H. Tian, and R. Yang. Preparation and electrocatalytic activity of 3D hierarchical porous spinel $CoFe_2O_4$ hollow nanospheres as efficient catalyst for oxygen reduction reaction and oxygen evolution reaction. *Electrochim. Acta*, 151:276–283, 2015. ISSN 00134686. doi:10.1016/j.electacta.2014.11.042.

[62] Y. Xu, W. Tu, B. Zhang, S. Yin, Y. Huang, M. Kraft, and R. Xu. Nickel nanoparticles encapsulated in few-layer nitrogen-doped graphene derived from metal-organic frameworks as efficient bifunctional electrocatalysts for overall water splitting. *Adv. Mater.*, 29(11):1605957, 2017. ISSN 1521-4095 (Electronic) 0935-9648 (Linking). doi:10.1002/adma.201605957. URL http://www.ncbi.nlm.nih.gov/pubmed/28102612.

[63] W. Yan, X. Cao, J. Tian, C. Jin, K. Ke, and R. Yang. Nitrogen/sulfur dual-doped 3d reduced graphene oxide networks-supported $CoFe_2O_4$ with enhanced electrocatalytic activities for oxygen reduction and evolution reactions. *Carbon*, 99:195–202, 2016. ISSN 00086223. doi:10.1016/j.carbon.2015.12.011.

[64] Z. Zhan, W.-N. Wang, L. Zhu, W.-J. An, and P. Biswas. Flame aerosol reactor synthesis of nanostructured SnO_2 thin films: High gas-sensing properties by control of morphology. *Sens. Actuators, B*, 150(2):609–615, 2010. ISSN 09254005. doi:10.1016/j.snb.2010.08.032.

[65] G. Zhang, J. Yang, H. Wang, H. Chen, J. Yang, and F. Pan. $Co_3O_{4-\delta}$ quantum dots as a highly efficient oxygen evolution reaction catalyst for water splitting. *ACS Appl. Mater. Interfaces*, 9(19):16159–16167, 2017. ISSN 1944-8252 (Electronic) 1944-8244 (Linking). doi:10.1021/acsami.7b01591. URL http://www.ncbi.nlm.nih.gov/pubmed/28447457.

[66] J. J. Zhang, H. H. Wang, T. J. Zhao, K. X. Zhang, X. Wei, Z. D. Jiang, S. I. Hirano, X. H. Li, and J. S. Chen. Oxygen vacancy engineering of Co_3O_4 nanocrystals through coupling with metal support for water oxidation. *ChemSusChem*, 10(14):2875–2879, 2017. ISSN 1864-564X (Electronic) 1864-5631 (Linking). doi:10.1002/cssc.201700779. URL http://www.ncbi.nlm.nih.gov/pubmed/28612461.

[67] W. Zhang, J. Qi, K. Liu, and R. Cao. A nickel-based integrated electrode from an autologous growth strategy for highly efficient water oxidation. *Adv. Energy Mater.*, 6(12):1502489, 2016. ISSN 16146832. doi:10.1002/aenm.201502489.

[68] Y. Zhang, Y. Liu, and M. Liu. Nanostructured columnar tin oxide thin film electrode for lithium ion batteries. *Chem. Mater.*, 18(19):4643–4646, 2006. ISSN 0897-4756 1520-5002. doi:10.1021/cm0519378.

[69] B. Zhao, K. Uchikawa, J. R. McCormick, C. Y. Ni, J. G. Chen, and H. Wang. Ultrafine anatase TiO_2 nanoparticles produced in premixed ethylene stagnation flame at 1atm. *Proc. Combust. Inst.*, 30(2):2569–2576, 2005. ISSN 15407489. doi:10.1016/j.proci.2004.08.146.

[70] F. Zheng. Thermophoresis of spherical and non-spherical particles: a review of theories and experiments. *Adv. Colloid Interface Sci.*, 97(1-3):255–278, 2002. ISSN 00018686. doi:10.1016/s0001-8686(01)00067-7.

[71] J. Zhou, Y. Dou, A. Zhou, R.-M. Guo, M.-J. Zhao, and J.-R. Li. MOF template-directed fabrication of hierarchically structured electrocatalysts for efficient oxygen evolution reaction. *Adv. Energy Mater.*, 7(12):1602643, 2017. ISSN 16146832. doi:10.1002/aenm.201602643.

[72] T. Zhou, Y. Du, S. Yin, X. Tian, H. Yang, X. Wang, B. Liu, H. Zheng, S. Qiao, and R. Xu. Nitrogen-doped cobalt phosphate@nanocarbon hybrids for efficient electrocatalytic oxygen reduction. *Energy Environ. Sci.*, 9(8):2563–2570, 2016. ISSN 1754-5692 1754-5706. doi:10.1039/c6ee01297c.

[73] T. Zhou, Y. Du, D. Wang, S. Yin, W. Tu, Z. Chen, A. Borgna, and R. Xu. Phosphonate-based metal-organic framework derived Co-P-C hybrid as an efficient electrocatalyst for oxygen evolution reaction. *ACS Catal.*, 7(9):6000–6007, 2017. ISSN 2155-5435 2155-5435. doi:10.1021/acscatal.7b00937.

[74] Y. P. Zhu, T. Y. Ma, M. Jaroniec, and S. Z. Qiao. Self-templating synthesis of hollow Co_3O_4 microtube arrays for highly efficient water electrolysis. *Angew. Chem., Int. Ed. Engl.*, 56(5):1324–1328, 2017. ISSN 1521-3773 (Electronic) 1433-7851 (Linking). doi:10.1002/anie.201610413. URL http://www.ncbi.nlm.nih.gov/pubmed/27900829.

[75] L. Zhuang, L. Ge, Y. Yang, M. Li, Y. Jia, X. Yao, and Z. Zhu. Ultrathin iron-cobalt oxide nanosheets with abundant oxygen vacancies for the oxygen evolution reaction. *Adv. Mater.*, 29(17):1606793, 2017. ISSN 1521-4095 (Electronic) 0935-9648 (Linking). doi:10.1002/adma.201606793. URL http://www.ncbi.nlm.nih.gov/pubmed/28240388.